

# A Fast and Effective Irregular Stripe Removal Method for Moon Mineralogy Mapper ( $M^3$ )

Shuheng Zhao, Qiangqiang Yuan<sup>✉</sup>, Member, IEEE, Jie Li<sup>✉</sup>, Member, IEEE, Yunze Hu,  
Xinxin Liu<sup>✉</sup>, and Liangpei Zhang<sup>✉</sup>, Fellow, IEEE

**Abstract**—Hyperspectral imagery (HSI) is one of the emerging tools to explore the physical properties and chemical composition of the lunar surface. Moon mineralogy mapper ( $M^3$ ) is the most widely used lunar HSI data set with the widest coverage and the excellent resolution; however, dense and nonperiodic stripes distributed across all bands in  $M^3$  images hinder visual interpretation as well as their use in subsequent applications. In this article, a fast despeckling approach for  $M^3$  is proposed using the Hodrick–Prescott decomposition embedded in the low-rank framework (LRHP) to overcome this limitation. The integration of a statistical filter and variational model tackles the problem stemming from a lack of the correct residual information when certain pixels are corrupted in every band, thereby restoring severely degraded hyperspectral images (HSIs). Simulated and real experiments conducted on typical regions on the Moon with various levels of corruption demonstrate that the proposed LRHP rapidly achieves favorable performance against state-of-the-art approaches. Also, expanding tests on interference imaging spectrometer (IIM) data of Chang’E-1 and commonly used terrestrial remote sensing images show that LRHP has good generalization capability. Moreover, the integrated band depth (IBD) maps further verify the necessity of despeckling and the high spectral fidelity of LRHP that benefits further applications.

**Index Terms**—Hodrick–Prescott (HP) decomposition, hyperspectral image despeckling, low-rank matrix restoration, Moon mineralogy mapper ( $M^3$ ).

Manuscript received August 27, 2020; revised December 11, 2020 and January 13, 2021; accepted January 19, 2021. This work was supported in part by the National Natural Science Foundation of China under Grant 41922008, Grant 61971319, Grant 61901166, and Grant 62071341; in part by the Hubei Science Foundation for Distinguished Young Scholars under Grant 2020CFA051; and in part by the Fundamental Research Funds for the Central Universities under Grant 531118010209. (Corresponding author: Qiangqiang Yuan.)

Shuheng Zhao is with the State Key Laboratory of Information Engineering in Surveying, Mapping and Remote Sensing, Wuhan University, Wuhan 430079, China (e-mail: shzhao@whu.edu.cn).

Qiangqiang Yuan is with the School of Geodesy and Geomatics, Wuhan University, Wuhan 430079, China, and also with the Collaborative Innovation Center of Geospatial Technology, Wuhan University, Wuhan 430079, China (e-mail: yqiang86@gmail.com).

Jie Li and Yunze Hu are with the School of Geodesy and Geomatics, Wuhan University, Wuhan 430079, China (e-mail: aaronleecool@whu.edu.cn; 2016301610220@whu.edu.cn).

Xinxin Liu is with the College of Electrical and Information Engineering, Hunan University, Changsha 410082, China (e-mail: liuxinxin@hnu.edu.cn).

Liangpei Zhang is with the State Key Laboratory of Information Engineering in Surveying, Mapping and Remote Sensing, Wuhan University, Wuhan 430079, China, and also with the Collaborative Innovation Center of Geospatial Technology, Wuhan University, Wuhan 430079, China (e-mail: zlp62@whu.edu.cn).

Color versions of one or more figures in this article are available at <https://doi.org/10.1109/TGRS.2021.3054661>.

Digital Object Identifier 10.1109/TGRS.2021.3054661

## I. INTRODUCTION

THE Moon was the first stop in the human interplanetary journey. Lunar detection is of great scientific significance for deepening our comprehension of the Earth–Moon system. Developing energy, minerals, and space environmental resources of the Moon and exploring the possibility as a future residence are the main targets of contemporary lunar exploration [1].

During the lunar surface detection process, we can acquire spatially coregistered images simultaneously with fine-scale spectrally contiguous bands via hyperspectral imaging. This technique provides a means to identify the chemical composition and analyze the physical states of minerals, rocks, and soil, but stripe noise commonly present on hyperspectral images (HSIs) limits their accuracy when used in subsequent applications [2], [3]. There are two main causes of stripe noises: limitations of sensor manufacturing and external disturbances. Hyperspectral imaging sensors are usually made up of push-broom linear charge-coupled device (CCD) arrays, and diverse photoelectric properties of each CCD lead to different spectral response functions, resulting in inconsistent responses to the input signal [4]–[6]. The other factor is that the unpredictable electromagnetic transformation disturbs the sensor during the movement of the remote sensing platform in space, exacerbating stripe noises [7], [8].

The Moon mineralogy mapper ( $M^3$ ) is an imaging spectrometer onboard the first Indian lunar probe Chandrayaan-1 and is operated by the National Aeronautics and Space Administration (NASA). It delivers high spatial and spectral resolution and covers 95% of the lunar surface [9]. However, its signal-to-noise ratio is affected by stripe noises due to sensor manufacturing limitations and the impact of the extraterrestrial environment [10]. Most  $M^3$  images are corrupted by severe nonperiodic and dense stripes, which are spread over every band with different spatial positions, intensities, and widths. Fig. 1 shows that the level of stripes varies across different bands in the  $M^3$  image. The presence of stripes will break the high correlation among bands, thereby interfering with the analysis through the spectral parameter maps and also reducing the accuracy of identification and extraction of surface material. Therefore, a stripe removal algorithm is needed for this special case.

Various despeckling approaches have been proposed to address different types of stripes. The existing methods can be roughly divided into three categories: filter-based

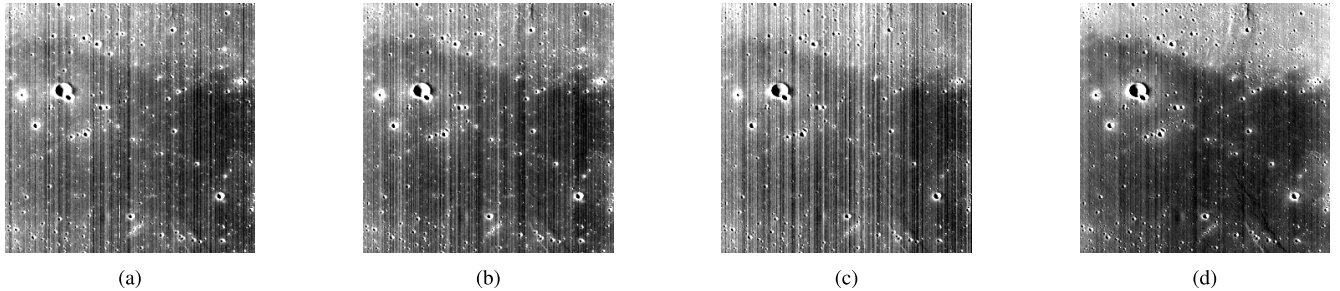


Fig. 1. Various distributions and intensities of stripes on  $M^3$ . Mare Imbrium: (a) Band 3, (b) Band 8, (c) Band 15, and (d) Band 50.

approaches, statistical-based approaches, and variational models [11].

Filter-based methods are the operations to exclude the specific frequency as the stripe component from the original signal [12], [13]. The most prevalent filters are the Fourier transform [12], [14], [15], the wavelet analysis [16], [17], and the combined wavelet-Fourier filters [5], [18]. These approaches have been adopted widely in the image restoration area due to their simplicity and have already achieved fast and impressive despeckling results, but they are not effective on nonperiodic stripes, which are hard to recognize and separate in the frequency domain. In addition, some useful signals are likely to be filtered out along with the stripes if a threshold is not selected properly. The loss of information will cause oversmooth and ringing artifacts in the spatial dimension.

Statistical methods are designed to correct a stripe-contaminated distribution to a reference distribution. Typical approaches are histogram matching [19], [20], equalization [4], [21], [22], moment matching [23], and so on. These kinds of approaches are popular because they balance between performance and efficiency and are generally applicable to regular stripes in homogeneous images. Nevertheless, they are not effective for HSIs with irregular stripes and will cause the spectral distortion as spectral correlation is not taken into consideration. Rakwatin *et al.* [24] combined the histogram matching with a facet filter to handle the stripes on the Moderate Resolution Imaging Spectroradiometer (MODIS) data, but this kind of model is still limited, if the strong similarity assumptions are invalid [25], [26].

As for variational models, despeckling is considered as an ill-posed inverse problem [27]. Aiming at the characteristics of stripes on HSIs, some competent regularizations, such as total variation [28]–[32], sparsity [33], [34], and low rank [35]–[37], are widely adopted to despeckle the whole HSI as a 2-D matrix or 3-D tensor [38]. These methods are effective, promising, and have strong generalization ability. However, it is challenging for them to deal with various stripes, and overcomplicated optimization model can be really time-consuming and meaningless for practical applications.

During recent years, the convolutional neural network (CNN) is widely applied to various low-level vision tasks of HSIs by a lot of researchers due to its excellent nonlinear fitting capability and automatic feature selection. Chang *et al.* [39] treated the image despeckling task as an image

decomposition problem and employed a two-stream CNN to handle it. Zhang *et al.* [40] employed a hybrid spatial-spectral gradient learning strategy based on spectral differences and spatial structure of noises to restore HSIs. Zhong *et al.* [11] adopted the satellite-ground integrated strategy to balance the training and test samples and then described both spatial and spectral degradations in real-world HSIs based on deep CNN. Although the CNN-based model outperformed conventional models, it lacks interpretability and relies heavily on training samples. So far, the generalization ability of deep learning networks is restricted on the study of the Moon because there are insufficient high-quality hyperspectral data for training. In addition, due to the largely different landcover between the Earth and the Moon, the effectiveness of transferring learning is also limited.

To sum up, although each method has its strength, most of them ignore the structural trait of stripes. In that case, neither strong (thick or intensive) stripes could be totally removed nor weak (thin or sparse) ones could be identified. Especially for several spatial-spectral hybrid despeckling models, which rely on the high correlation among bands of HSIs, they often fail to achieve fulfilling results when the image is corrupted too much to provide enough information for recovery. Given the intensity and positions of dense stripes of  $M^3$  vary among different bands, the high correlation inside it will be undermined, and there is a large possibility that certain columns of all the bands will be contaminated by stripes, thereby undermining the high correlation inside  $M^3$ . To address this problem, a new algorithm aimed at the lunar hyperspectral data set is developed. In this article, the main innovations can be generalized as follows.

- 1) We propose a novel and first despeckling model targeting at lunar hyperspectral data sets, which can jointly estimate the image component and the stripe component, thereby accelerating convergence.
- 2) In light of the consistent vertical characteristic of stripes which can be implicitly described in the mean cross-track profile on  $M^3$  images, a directional statistical restriction embedded in the low-rank recovery framework can better and more precisely identify the spatial distribution of stripes, even those with low contrast to the context, and guide the overall optimization with the high spectral fidelity.
- 3) Extensive experiments and the integrated band depth (IBD) mapping results confirmed that the

proposed model exhibits both a competitive effectiveness especially for seriously corrupted lunar HSIs and a high efficiency and when compared with other state-of-the-art approaches.

The remainder of this article is organized as follows. In Section II, the proposed destriping model is introduced at great length. In Section III, more details about the M<sup>3</sup> data set are given along with experimental results. A discussion about the generalization capability of the proposed model and a spectral analysis are given in Section IV. Finally, conclusions and future work are shown in Section V.

## II. METHODOLOGY

In this section, the proposed low-rank matrix recovery with embedded single-band Hodrick–Prescott decomposition (LRHP) destriping method and its optimization are presented in detail. First, the Hodrick–Prescott (HP) decomposition is utilized to estimate the ideal statistic distribution of the clear image, and then, the smooth profile is employed as the guidance for low-rank constraints on the HSI to make up the overall regularization term of the image. Meanwhile, the stripe component is leveraged by the low-rank prior based on its directional characteristics so as to separate it from the HSI efficiently.

### A. Degradation Formulation

Assuming that all the stripes on M<sup>3</sup> can be regarded as the additive noise [28], thus the stripe-contaminated model can be expressed as

$$\mathbf{Y} = \mathbf{X} + \mathbf{S} \quad (1)$$

where  $\mathbf{Y}$  is the observed HSI,  $\mathbf{X}$  is the desired clean HSI, and  $\mathbf{S}$  denotes the stripe component.  $\mathbf{Y}$ ,  $\mathbf{X}$ , and  $\mathbf{S}$  are 3-D cubes with the same size of  $M \times N \times B$ , where  $M$ ,  $N$ , and  $B$  denote the width, the height, and the number of channels, respectively. Then, the destriping model for M<sup>3</sup> can be expressed as a regularization-based problem

$$\hat{\mathbf{X}} = \arg \min_{\mathbf{X}, \mathbf{S}} R_1(\mathbf{X}) + \alpha R_2(\mathbf{S}) + \frac{\beta}{2} \|\mathbf{Y} - \mathbf{X} - \mathbf{S}\|_2^2. \quad (2)$$

In (2),  $R_1(\mathbf{X})$  and  $R_2(\mathbf{S})$  stand for the regularization terms, which provide prior knowledge to the optimization process.  $\|\mathbf{Y} - \mathbf{X} - \mathbf{S}\|_2^2$  is the data-fidelity term, indicating the fidelity between the estimated result and the observed image. The terms  $\alpha$  and  $\beta$  are the regularization parameters, which balance the contributions of the regularization terms and data fidelity. The key problem was developing a means to exploit prior distribution and design regularization terms for both  $\mathbf{X}$  and  $\mathbf{S}$ . This will be discussed in Section II-B.

### B. Regularizations Design

1) *Prior Exploration for the HSI*: Recently, low-rank matrix approximation has become common in HSI restoration tasks [41], [42]. The low-rank matrix recovery (LRMR) model was first put forward by Wright *et al.* [43]. Zhou *et al.* [44] improved their study and applied it to recover

the high-dimensional matrix corrupted by sparse noises. In Zhang *et al.* [40] adopted the LRMR model for HSI destriping and obtained satisfactory results by rearranging the HSI as a 2-D Casorati matrix and exploring its low-rank properties using linear spectral mixing models [45]. This kind of prior models can fully utilize the redundancy and correlations in both spatial and spectral dimensions simultaneously, thereby suppressing the spectral distortion effectively

$$R_1(\mathbf{X}) = \text{rank}(\mathcal{X}) \quad \text{s.t. } \mathcal{X} = C(\mathbf{X}) \quad (3)$$

where  $\mathcal{X}$  denotes the Casorati matrix of the clean HSI  $\mathbf{X}$ . However, the optimization of regularization as (3) is NP-hard due to the discrete nature of the rank [46], and it can be relaxed via replacing by the nuclear norm

$$R_1(\mathbf{X}) = \|\mathcal{X}\|_* \quad \text{s.t. } \mathcal{X} = C(\mathbf{X}) \quad (4)$$

where the expression of the nuclear norm is

$$\|\mathcal{X}\|_* = \text{tr}(\sqrt{\mathcal{X}^T \mathcal{X}}). \quad (5)$$

HSIs with relatively low-level noise can be effectively restored based on the low-rank prior, but M<sup>3</sup> is affected by relatively severe stripes distributed across all bands. The high correlation between each band inside the HSI will be corrupted, thereby making the performance of the LRMR model unsatisfactory. To eliminate this corruption, we exploit the structure of the stripes and apply statistical prior distribution to every single band for guidance in the low-rank optimization framework. Since the stripes of M<sup>3</sup> have directionality, they can be visualized as a vertical profile [15], [47] like the images shown in Fig. 2.

As shown in Fig. 2(d), the mean vertical profile of the nearly clean M<sup>3</sup> data obtained in the early stage is smooth, while the curve after adding simulated stripes fluctuates as in Fig. 2(f); however, the curves of the clean image and the striped image share the same trend. Inspired by this phenomenon, the HP decomposition can be used to estimate the distribution of the nonperiodic stripe components on every single band.

The HP decomposition, also known as the HP filter, is commonly used in macroeconomics for time series analysis [48], [49]. It can separate a cyclical component from the raw data series, thereby filtering nonperiodic parts. Recalling that the stripes of M<sup>3</sup> are nonperiodic, hence, using the HP decomposition can filter the dense and nonperiodic components to obtain a smooth profile that can be regarded as a reference for the subsequent low-rank recovery framework.

The embedded HP decomposition can guide the low-rank recovery framework when the correlation among bands inside the HSI is damaged. For the convenience of calculation, the input image needs to be rotated 90°, and then, the stripes become horizontal. In each band, the HP decomposition is conducted as [50], [51]

$$\hat{\mathbf{h}}_i = \arg \min_{\mathbf{h}_i} \left\{ \frac{1}{g} \left\| \hat{\mathbf{h}}_i - \mathbf{Y}_i \mathbf{c} \right\|_g^g + \frac{\lambda_{\text{gp}}}{2} \left\| \mathbf{G} \mathbf{h}_i \right\|_2^2 \right\} \quad (6)$$

where  $\mathbf{Y}_i$  is the  $i$ th band of the observed HSI,  $\mathbf{c} \in R^{N \times 1}$  is an operator whose elements are all equal to  $1/N$ , and  $\mathbf{Y}_i \mathbf{c}$  denotes the mean cross-track profile of  $\mathbf{Y}_i$ .  $\mathbf{G}$  is the Gaussian

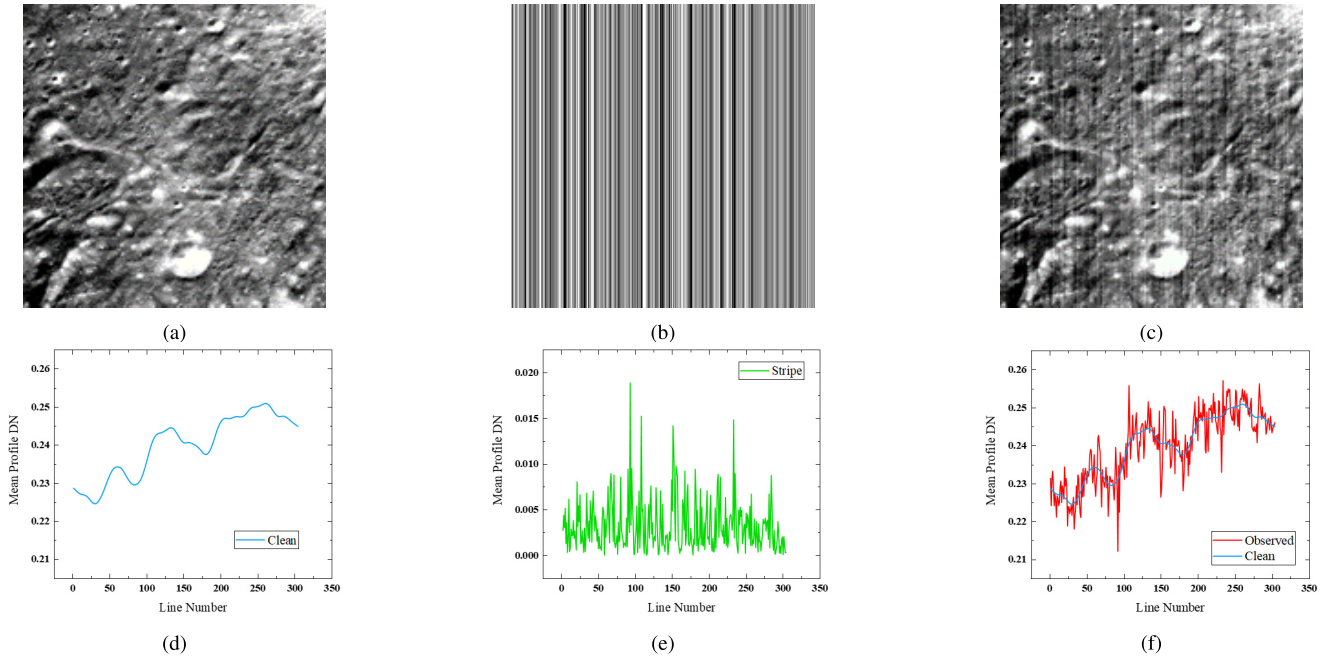


Fig. 2. Mean cross-track profile of clean image and striped image. (a) Clean image. (b) Simulated stripes. (c) Degraded image. (d) Mean cross-track profile of (a). (e) Mean cross-track profile of (b). (f) Mean cross-track profile of (c).

blur kernel  $[1 \ -2 \ 1]^T$ ,  $\hat{\mathbf{h}}_i \in R^{M \times 1}$  is the estimated profile, and  $\lambda_{gp}$  is the regularization parameter that controls the smooth degree of  $\hat{\mathbf{h}}$ . Note that  $g \in [1, 2]$  is an integer, and  $g = 1$  is more suitable when the  $M^3$  image was obtained in the early stage of its mission and only slightly corrupted by the stripes, whereas  $g = 2$  fits in cases when the stripes are densely distributed. To get the reference  $\hat{\mathbf{h}}$ , the weighted least-squares minimization [4], [52] is adopted for iteration

$$\hat{\mathbf{h}}_i^{k+1} = \arg \min \left\{ \frac{1}{2} \left\| \sqrt{\mathbf{W}_i^k} (\mathbf{h}_i - \mathbf{Yc}) \right\|_2^2 + \frac{\lambda_{gp}}{2} \|\mathbf{Gc}\|_2^2 \right\} \quad (7)$$

where  $\mathbf{W}$  is the weight matrix

$$\mathbf{W}_i^k = \begin{cases} \text{diag}|\mathbf{h}_i^k - \mathbf{Yc}|^{g-2}, & \text{if } |\mathbf{h}_i^k - \mathbf{Yc}| > z \\ \text{diag}|z|^{g-2}, & \text{if } |\mathbf{h}_i^k - \mathbf{Yc}| \leq z \end{cases} \quad (8)$$

and  $z$  is a small positive constant. The estimated smooth profile can be solved as

$$\hat{\mathbf{h}}_i^{k+1} = (\mathbf{W}_i^k + \lambda_{gp} \mathbf{G}^T \mathbf{G})^{-1} \mathbf{W}_i^k \mathbf{Y}_i \mathbf{c}. \quad (9)$$

After gaining the estimated smooth profile of every single band, we integrate it with the low-rank prior to make up the whole regularization term for  $\mathbf{X}$

$$R_1(\mathbf{X}) = \|\mathcal{X}\|_* + \lambda_1 \sum_{i=1}^B \left\| \hat{\mathbf{h}}(\mathbf{Y}_i) - \mathbf{X}_i \mathbf{c} \right\|_2^2 \quad \text{s.t. } \mathcal{X} = C(\mathbf{X}) \quad (10)$$

where  $\lambda_1$  is the regularization parameter,  $\mathbf{Y}_i$  is the  $i$ th band of the clean HSI, and  $\|\hat{\mathbf{h}}(\mathbf{Y}_i) - \mathbf{X}_i \mathbf{c}\|_2^2$  is the data-fidelity term of each band.

**2) Prior Exploration for the Stripe Component:** Different from methods that concentrate on the properties of the image and approaches focused on estimating the stripe component with less consideration on the image, Chang *et al.* [26] treated the image and stripes equally and decoupled them completely to avoid loss of detail. After quantitatively analyzing the stripes in various remote sensing images, they found that the rank of stripes is absolutely lower than images. Therefore, the subspace spanned by the additive stripes can be well described as low-rank.

Based on [26], we analyze the rank of stripes on  $M^3$ . The stripe component in Fig. 3(c) is extracted via the wavelet-Fourier adaptive filter (WFAF) [5]. It can be seen from Fig. 3(d) that the singular values of the stripe component decrease rapidly to zero at rank 1, and thus, we think that the low-rank prior is suitable for stripes. Considering that the stripes on  $M^3$  images are densely and globally distributed with clear directionality, then the low-rank-induced nuclear norm is more appropriate than the L1-norm [26], [43]. Stripes on different bands have varying intensities and distributions; we chose to impose low-rank constraints on each band for higher quality results. Taking all the aforementioned considerations into account, the low-rank-induced nuclear norm on every single band is selected to constraint the stripe component

$$\alpha R_2(\mathbf{S}) = \lambda_2 \sum_{i=1}^B \|\mathbf{S}_i\|_* \quad (11)$$

where  $\mathbf{S}_i$  is the  $i$ th band of the striped component and  $\lambda_2$  is the regularization parameter.

**3) Integrated LRHP Model:** After designing match restrictions for the HSI and the stripe component, the overall model

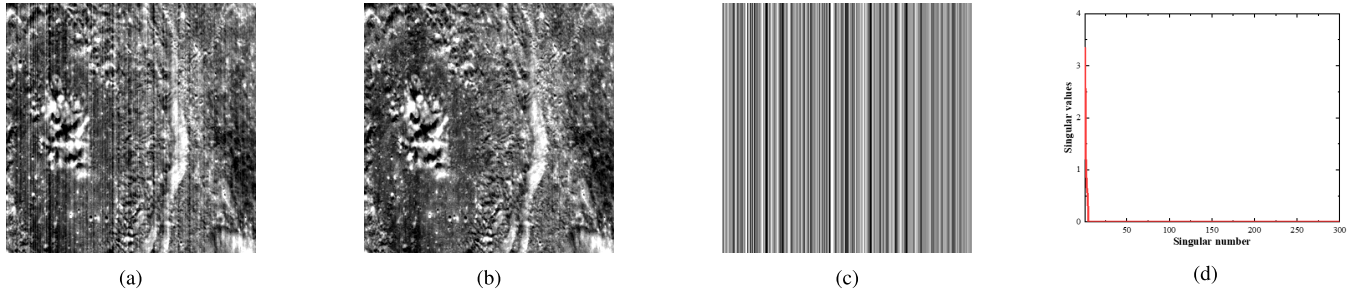


Fig. 3. Low-rank analysis of stripes on M<sup>3</sup>. (a) Finsen Crater: band 15. (b) Destriped by WFAF. (c) Stripe component. (d) Singular value of (c).

can be expressed as

$$\begin{aligned} (\hat{\mathbf{X}}, \hat{\mathbf{S}}) = & \arg \min_{\mathbf{X}, \mathbf{S}} \|\mathcal{X}\|_* + \lambda_1 \sum_{i=1}^B \left\| \hat{\mathbf{h}}(\mathbf{Y}_i) - \mathbf{X}_i \mathbf{c} \right\|_2^2 \\ & + \lambda_2 \sum_{i=1}^B \|\mathbf{S}_i\|_* + \sum_{i=1}^B \frac{\beta}{2} \left\| \mathbf{Y}_i - \mathbf{X}_i - \mathbf{S}_i \right\|_2^2 \\ \text{s.t. } & \mathcal{X} = C(\mathbf{X}). \end{aligned} \quad (12)$$

In (12), the HSI and the stripe component are treated equally, and thereby, they can be estimated iteratively.

### C. Optimization Procedure

To solve the minimization model (12), one auxiliary variable  $\mathbf{P} \in R^{M \times N \times B}$  is introduced to facilitate the calculation and avoid confusion, and thus, we can obtain

$$\begin{aligned} (\hat{\mathbf{X}}, \hat{\mathbf{S}}) = & \arg \min_{\mathbf{X}, \mathbf{S}} \|\mathbf{P}\|_* + \lambda_1 \sum_{i=1}^B \left\| \hat{\mathbf{h}}(\mathbf{Y}_i) - \mathbf{X}_i \mathbf{c} \right\|_2^2 \\ & + \lambda_2 \sum_{i=1}^B \|\mathbf{S}_i\|_* + \sum_{i=1}^B \frac{\beta}{2} \left\| \mathbf{Y}_i - \mathbf{X}_i - \mathbf{S}_i \right\|_2^2 \\ \text{s.t. } & \mathbf{P} = \mathcal{X}. \end{aligned} \quad (13)$$

Then, the Lagrangian function of (13) is

$$\begin{aligned} \mathcal{L}(\mathbf{P}, \mathbf{X}, \mathbf{S}, \mathbf{J}) = & \|\mathbf{P}\|_* + \lambda_1 \sum_{i=1}^B \left\| \hat{\mathbf{h}}(\mathbf{Y}_i) - \mathbf{X}_i \mathbf{c} \right\|_2^2 \\ & + \lambda_2 \sum_{i=1}^B \|\mathbf{S}_i\|_* + \sum_{i=1}^B \frac{\beta}{2} \left\| \mathbf{Y}_i - \mathbf{X}_i - \mathbf{S}_i \right\|_2^2 \\ & + \langle \mathbf{J}, \mathbf{P} - \mathcal{X} \rangle + \frac{\mu}{2} \|\mathbf{P} - \mathcal{X}\|_2^2 \end{aligned} \quad (14)$$

where  $\langle \cdot, \cdot \rangle$  represents the inner product operator,  $\mathbf{J} \in R^{(M \times N) \times B}$  is the Lagrange multiplier, and  $\mu$  denotes the penalty parameter. To solve the proposed model (14) efficiently, the alternating direction method of multiplier (ADMM) [53] is applied. The optimization of (14) can be divided into  $\mathbf{P}$ ,  $\mathbf{X}$ , and  $\mathbf{S}$ , three subproblems. After the regularization and initialization parameters are suitably selected, the variables can be updated one by one in the  $k$ th iteration as follows.

#### 1) Update $\mathbf{P}$ .

The  $\mathbf{P}$ -related subproblem can be expressed as

$$\begin{aligned} \mathbf{P}^{k+1} = & \arg \min_{\mathbf{P}} \|\mathbf{P}\|_* + \langle \mathbf{J}^k, \mathbf{P} - \mathcal{X}^k \rangle + \frac{\mu}{2} \|\mathbf{P} - \mathcal{X}^k\|_2^2 \\ = & \arg \min_{\mathbf{P}} \|\mathbf{P}\|_* + \frac{\mu}{2} \|\mathbf{P} - \mathcal{X}^k + \mathbf{J}^k / \mu\|_2^2. \end{aligned} \quad (15)$$

Equation (15) is a typical nuclear norm regularized least-squares problem with a closed-form solution. It can be solved by the singular value thresholding (SVT) operation [54]

$$\begin{cases} \mathbf{P}^{k+1} = \mathbf{U}_{\mathbf{P}}(\text{shrink\_L} * (\sum_{\mathbf{p}}, 1/\mu)) \mathbf{V}_{\mathbf{P}}^T \\ \text{shrink\_L} * (\sum_{\mathbf{p}}, 1/\mu) = \text{diag}\left\{\max\left(\sum_{\mathbf{p}_{ii}} - 1/\mu, 0\right)\right\} \end{cases} \quad (16)$$

where  $\mathcal{X} - \mathbf{J} = \mathbf{U}_{\mathbf{P}} \sum_{\mathbf{p}} \mathbf{V}_{\mathbf{p}}^T$  is the singular value decomposition of  $\mathcal{X}^k - \mathbf{J}^k$  and  $\sum_{\mathbf{p}_{ii}}$  is the diagonal element of the singular value matrix  $\sum_{\mathbf{p}}$ .

#### 2) Update $\mathbf{S}$ .

The  $\mathbf{S}$ -related subproblem is given by

$$\mathbf{S}^{k+1} = \arg \min_{\mathbf{S}} \lambda_2 \sum_{i=1}^B \|\mathbf{S}_i\|_* + \frac{\beta}{2} \|\mathbf{Y}_i - \mathbf{X}^k - \mathbf{S}_i\|_2^2. \quad (17)$$

Equation (17) is also a low-rank matrix approximation problem that has a closed-form solution, so the SVT operation is employed again

$$\begin{cases} \mathbf{S}_i^{k+1} = \mathbf{U}_{\mathbf{S}_i}(\text{shrink\_L} * (\sum_{\mathbf{S}_i}, \lambda_2 / \beta)) \mathbf{V}_{\mathbf{S}_i}^T \\ \text{shrink\_L} * (\sum_{\mathbf{S}_i}, \lambda_2 / \beta) \\ = \text{diag}\left\{\max\left(\sum_{\mathbf{S}_{ii}} - \lambda_2 / \beta, 0\right)\right\}. \end{cases} \quad (18)$$

Likewise,  $\mathbf{Y}_i - \mathbf{X}_i = \mathbf{U}_{\mathbf{S}_i} \sum_{\mathbf{S}_i} \mathbf{V}_{\mathbf{S}_i}^T$  represents the singular value decomposition of  $\mathbf{Y}_i - \mathbf{X}_i^k$  and  $\sum_{\mathbf{S}_{ii}}$  denotes the diagonal element of  $\sum_{\mathbf{S}_i}$ .

#### 3) Update $\mathbf{X}$ .

The  $\mathbf{X}$ -related subproblem can be obtained through fixing the other variables as follows:

$$\begin{aligned} \mathbf{X}^{k+1} = & \arg \min_{\mathbf{X}} \lambda_3 \sum_{i=1}^B \left\| \hat{\mathbf{h}}(\mathbf{Y}_i) - \mathbf{X}_i \mathbf{c} \right\|_2^2 \\ & + \frac{\beta}{2} \left\| \mathbf{Y}_i - \mathbf{X}_i - \mathbf{S}_i^k \right\|_2^2. \end{aligned} \quad (19)$$

**Algorithm 1** LRHP Solver for M<sup>3</sup> Data Set Destriping

**Input:** Original M<sup>3</sup> datacube  $\mathbf{Y}$ ,  $g$  (1 for sparse stripes, 2 for dense stripes), MaxIter,  $k$ , regularization parameters:  $\lambda_{gp}$ ,  $\lambda_1$ ,  $\lambda_2$  and  $\beta$ .

**Initialize:**  $\mathbf{P}_0 = \mathcal{X}$ ,  $\mathbf{X}_0 = \mathbf{Y}$ ,  $\mathbf{S}_0 = 0$ ,  $\mathbf{J}_0 = 0$ ,  $k = 0$

While  $\|\mathbf{Y} - \mathbf{X}^k - \mathbf{S}^k\|_F / \|\mathbf{Y}\|_F > \delta$  and  $k < \text{MaxIter}$  do

Update  $\mathbf{P}$  by solving Eq.(16).

Update  $\mathbf{S}$  by solving Eq.(18).

Update  $\mathbf{X}$  by solving Eq.(20).

Update the multiplier  $\mathbf{J}$  by solving Eq.(21).

end while

**Output:** Destriped M<sup>3</sup> datacube  $\mathbf{X}$  and the stripe component  $\mathbf{S}$ .

Since the HP decomposition of each band is different, the solution of  $\mathbf{X}$  is bandwise. It is also a least-squares problem and can be settled by

$$\mathbf{X}_i^{k+1} = [2\lambda_3 \hat{\mathbf{h}}(\mathbf{Y}_i) \mathbf{c}^T + \beta(\mathbf{Y}_i - \mathbf{S}_i^k)] [2\lambda_3 \mathbf{c} \mathbf{c}^T + \beta \mathbf{I}_N]^T \quad (20)$$

where  $\mathbf{I}_N$  is an identity matrix of size  $N \times N$ .

4) Update the multiplier  $\mathbf{J}$ .

The Lagrange multiplier is updated as

$$\mathbf{J}^{k+1} = \mathbf{J}^k + \mu(\mathbf{P}^k - \mathcal{X}^k). \quad (21)$$

Summarizing the above procedure, the ADMM algorithm optimizes the proposed model in Algorithm 1. In addition,  $\mu$ , the penalty parameter, is adaptatively updated via the method in [55] to facilitate the convergence.

### III. EXPERIMENTS AND ANALYSIS

#### A. Experimental Data

The M<sup>3</sup> is a lunar hyperspectral-imaging sensor developed by NASA and Brown University. It was loaded on the Indian Chandrayaan-1 and launched on October 1, 2008. M<sup>3</sup> made its biggest discovery in 2009 for finding the existence of water molecules in the polar regions of Moon [9], [10]. It can obtain HSIs from visible to near-infrared wavelength, covering 420–3000 nm. M<sup>3</sup> has two operating modes: the target mode and global mode. Under the target mode, the spatial resolution of gained HSIs is 80 m/pixel with 255 bands. While the images acquired under the global mode have 85 bands, the spatial resolution is 140 m/pixel. Albeit the spatial resolution of images under the target mode is higher, their quantity is very limited. On the contrary, HSIs under global mode cover 95% of the lunar surface. They have made outstanding contributions to the research of lunar minerals and greatly improved the applications of relevant data, such as geological composition data, photometry, and thermal radiation data. In this article, the reflectance data under global mode after photometrical correction is adopted. Also, the special research regions used in the simulated and real experiments will be introduced in Sections III-C and III-D, respectively.

#### B. Experimental Settings

Both simulated and real experiments were carried out to illustrate the effectiveness of LRHP. Six state-of-the-art algorithms were chosen for intercomparison: the WFAF [5], the anisotropic spectral–spatial total variation (ASSTV) [30], the low-rank-based single-image decomposition (LRID) model [26], the low-rank tensor decomposition destriping (LRTD) model [36], the local low-rank matrix recovery and global spatial–spectral total variation (LLRGTV) [56], and the nonindependent and identically mixture of Gaussians (NMog) noise assumption [57]. The links of the selected algorithms and the proposed model will be organized and uploaded to the author's Github (<https://github.com/photonmango>).

In the following experiments, the parameters involved in the compared approaches were manually tuned according to their default settings to the optimal. As for the proposed LRHP, the discussion of parameters will be shown in Section III-E. All experiments were conducted using MATLAB R2019b on a PC equipped with Intel Xeon E5-2620 CPU (at 2.10 GHz) and 16-GB RAM.

#### C. Simulated Experiments

The M<sup>3</sup> observation M3G20081122T232908 obtained in the early stage with less degradation was selected for a fact-based simulation. After further filtering out the bands that contain a small portion of noises, a clean 300 × 300 × 55 HSI cube covering 1089–2976 nm for simulated experiments was obtained. The gray values of the data were normalized to [0,1] before simulated experiments and reverted to the original level after destriping.

In order to evaluate the destriping performance of simulated experiments in both the spatial and spectral domain, six quantitative criteria are introduced as follows.

1) Mean peak signal-to-noise ratio (MPSNR) [58]

$$\text{MPSNR} = \frac{1}{B} \sum_{k=1}^B 10 \lg \frac{M \times N \times A^2}{\sum_{i=1}^M \sum_{j=1}^N (x(i, j, k) - y(i, j, k))^2} \quad (22)$$

where  $M$ ,  $N$ , and  $B$  represent the HSI's width, height, and number of bands, respectively,  $A$  is the maximum value of all the gray values,  $x(i, j, k)$  denotes the estimated image, and  $y(i, j, k)$  stands for the original clean image.

2) Mean structural similarity index (MSSIM) [59]

$$\text{MSSIM} = \frac{1}{B} \sum_{i=1}^B \frac{(2\mu_{x_i} \mu_{y_i} + C_1)(2\sigma_{x_i y_i} + C_2)}{(\mu_{x_i}^2 + \mu_{y_i}^2 + C_1)(\sigma_{x_i}^2 + \sigma_{y_i}^2 + C_2)} \quad (23)$$

where  $\mu_{x_i}$  and  $\mu_{y_i}$  stand for the mean values of the  $i$ th estimated and original clean image, respectively,  $\sigma_{x_i}^2$  and  $\sigma_{y_i}^2$  are the variances,  $\sigma_{x_i y_i}$  is the covariance, and  $C_1$  and  $C_2$  are constants that prevent the denominator from being 0. The mean value of SSIM of each band is adopted to assess the structural similarity of the whole.

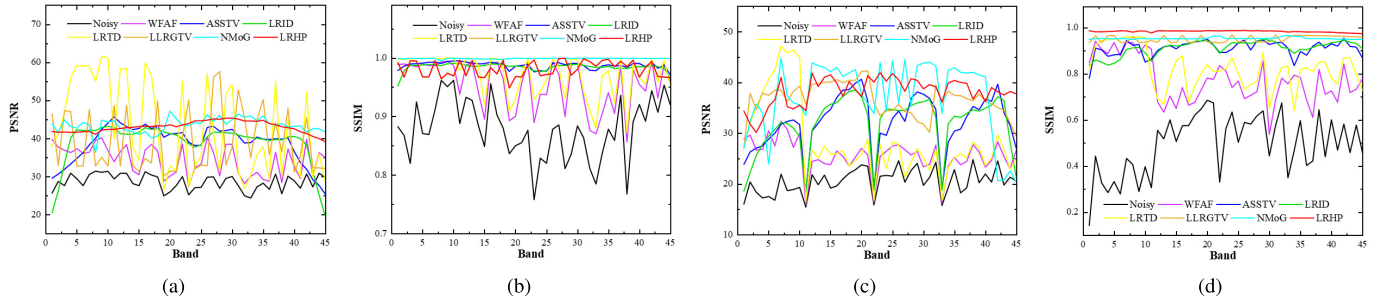


Fig. 4. PSNR and SSIM values of each band. (a) PSNR values under Case 1. (b) SSIM values under Case 1. (c) PSNR values under Case 2. (d) SSIM values under Case 2.

### 3) Absolute skewness (Askew)

Askew

$$= \left| \frac{\sum_{i=1}^M \sum_{j=1}^N \sum_{k=1}^B (x(i, j, k) - y(i, j, k))^3 / MNB}{\left( \sqrt{\sum_{i=1}^M \sum_{j=1}^N \sum_{k=1}^B (x(i, j, k) - y(i, j, k))^2 / MNB} \right)^3} \right|. \quad (24)$$

The skewness describes the symmetry of the overall value distribution of samples; in other words, it is used to assess the distortion of the estimated results compared with the original sample. The smaller the absolute value of skewness is, the closer the estimated image is to the original image.

### 4) Absolute kurtosis (Akurt)

Akurt

$$= \left| \frac{\sum_{i=1}^M \sum_{j=1}^N \sum_{k=1}^B (x(i, j, k) - y(i, j, k))^4 / MNB}{\left( \sum_{i=1}^M \sum_{j=1}^N \sum_{k=1}^B (x(i, j, k) - y(i, j, k))^2 / MNB \right)^2} \right|. \quad (25)$$

It is sometimes quite hard to distinguish between noise and image content, especially in some regions that have low contrast textures. The absolute kurtosis can make a statement of how good a denoising algorithm works on that. When the spatial resolution is constant, the lower Akurt value shows less noise remained on the image.

### 5) Mean spectral angle mapper (MSAM) [60]

$$\text{MSAM} = \frac{1}{MN} \cos^{-1} \left[ \frac{\sum_{i=1}^{MN} t_i p_i}{\sqrt{\left( \sum_{i=1}^{MN} t_i^2 \right) \left( \sum_{i=1}^{MN} p_i^2 \right)}} \right] \quad (26)$$

where  $t_i$  denotes the estimated spectrum and  $p_i$  is the original spectrum. This metric is adopted to assess the spectral fidelity of destriping algorithms.

### 6) Pearson product-moment correlation coefficient ( $r$ )

$$r = \frac{\sum_{i=1}^{MN} (t_i - \bar{t})(p_i - \bar{p})}{\sqrt{\sum_{i=1}^{MN} (t_i - \bar{t})^2} \sqrt{\sum_{i=1}^{MN} (p_i - \bar{p})^2}} \quad (27)$$

where  $\bar{t}$  denotes the average of all estimated spectra and  $\bar{p}$  is the mean spectrum of original spectra. This numeric quantity is also used to measure the interband spectral correlation.

Better destriping results correspond to higher MPSNR, MSSIM, and  $r$  and lower Askew, Akurt, and MSAM.

Since M<sup>3</sup> images are only corrupted with stripes, other types of noise were not considered during simulated experiments. Two cases were simulated as follows.

1) *Case 1 (Sparse Stripes)*: Both global and partial stripes with intensity between 0 and 0.05 were added randomly to 50% bands of the HSI. The purpose of this simulation is to model cases when a few M<sup>3</sup> images acquired in the early stage are slightly corrupted and to test the ability to remove different types of stripes.

2) *Case 2 (Dense Stripes)*: In this case, various stripes, such as periodic, nonperiodic, partial, and thick stripes, were added randomly into every band of the HSI. Given that the intensity of the stripes varies among different bands because of the unbalanced incidental light, the intensity was randomly selected within a range from 0.1 to 0.5 randomly in each band. This case is closer to a scenario where most of the M<sup>3</sup> images obtained in the later stage are degraded more severely.

1) *Quantitative Comparison*: Fig. 4 presents the peak signal-to-noise ratio (PSNR) and SSIM values for each band as produced by different approaches in Case 1 and 2. When the stripes are sparse, NMoG and LRHP yield relatively high and stable PSNRs than the other methods. Although LRTD and LLRGTV achieve very high PSNRs for some bands, their performance in the other bands is unsatisfactory, thereby causing the overall trend to fluctuate. As for the SSIMs values in Fig. 4(b), in addition to WFAF, the other approaches have stable and high SSIMs, among which NMoG is the top performer. When the stripes are dense, LLRGTV, NMoG, and LRHP still obtain high PSNR and SSIM values, but LRHP is the most stable approach and delivered the highest SSIMs.

The quantitative evaluation indicators for the destriping results are listed in Table I, in which the best results are marked in bold, and the second ones are underlined.

In Case 1, it can be found that all these methods except for WFAF can remove most of the sparse stripes. Among these algorithms, NMoG outperforms the other tested algorithms, while the proposed LRHP model is the second, but LRHP has an absolute advantage over NMoG in terms of running time. We think that there are two main reasons why LRHP does not obtain the best indicators when the stripes are sparse. First, due to the design error of simulated experiments, there are

TABLE I  
PERFORMANCE COMPARISON OF SIMULATED EXPERIMENTS ON ALL COMPETING METHODS

Case 1: sparse stripes								
Index	Noisy	WFAF	ASSTV	LRID	LRTD	LLRGTV	NMoG	LRHP
MPSNR	28.5387	34.3678	38.7004	38.8794	42.8862	39.2242	<b>45.4550</b>	<u>44.3061</u>
MSSIM	0.8781	0.9547	0.9872	0.9842	0.9707	0.9809	<b>0.9988</b>	<u>0.9928</u>
Askew	1.2233	1.3918	<u>1.0825</u>	1.1697	1.2183	<b>1.0530</b>	1.1898	1.1960
Akurt	1.3416	1.2409	1.7798	2.1836	1.3857	1.8606	<b>0.7946</b>	<u>0.9915</u>
MSAM	4.2780	2.6108	2.2940	3.5280	1.6905	1.1786	<b>0.1817</b>	<u>0.4835</u>
$r$	0.8562	0.9613	0.9828	0.9495	0.9681	0.9766	<b>0.9998</b>	<u>0.9974</u>
Time/s	-	<b>4.97</b>	27.15	273.18	113.65	94.01	108.64	<u>9.56</u>
Case 2: dense stripes								
Index	Noisy	WFAF	ASSTV	LRID	LRTD	LLRGTV	NMoG	LRHP
MPSNR	20.4607	25.5723	32.2246	31.8053	28.2231	36.5381	<u>37.4018</u>	<b>38.0207</b>
MSSIM	0.4937	0.7733	0.9106	0.9118	0.8229	0.9518	<u>0.9536</u>	<b>0.9867</b>
Askew	1.3942	1.3981	1.3237	1.3208	<u>1.2960</u>	1.4790	1.4157	<b>0.0325</b>
Akurt	0.4024	0.9793	0.9855	0.9911	0.8861	<u>0.2844</u>	0.2898	<b>0.0611</b>
MSAM	12.7123	27.7809	<u>4.5794</u>	5.5212	7.1846	4.6250	4.7940	<b>1.6811</b>
$r$	0.6277	0.8867	0.8928	0.8566	0.7936	0.8942	<u>0.8954</u>	<b>0.9860</b>
Time/s	-	<b>4.88</b>	79.57	835.84	294.31	354.75	194.36	<u>10.12</u>

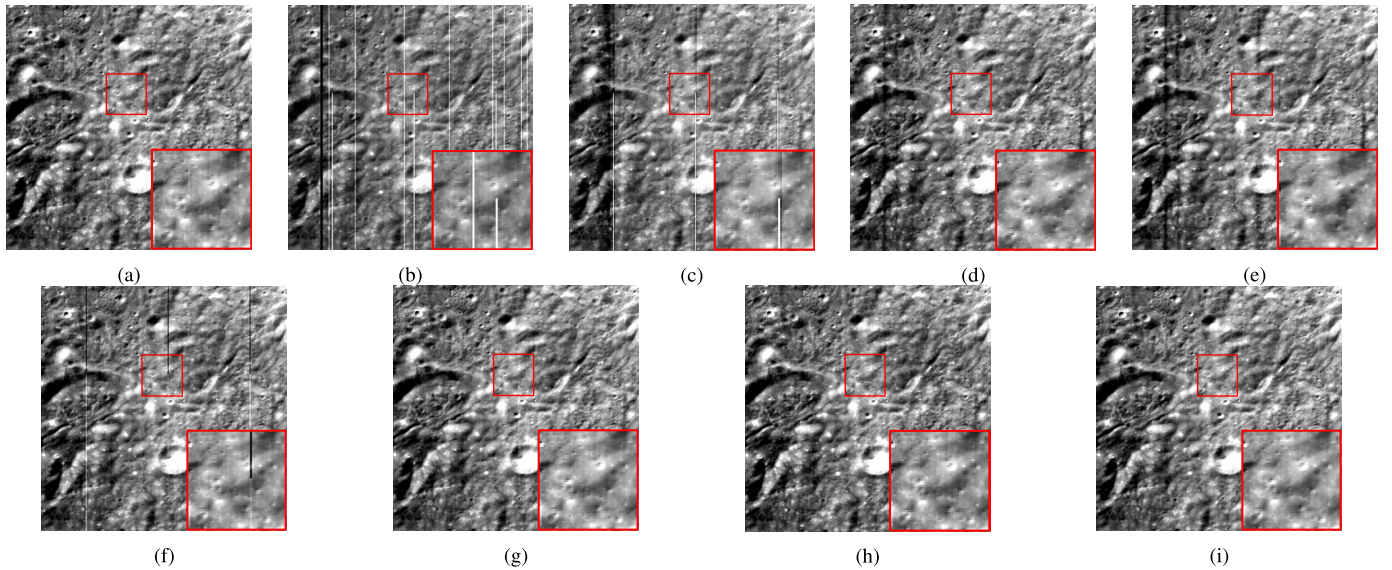


Fig. 5. Destripping results for simulated  $M^3$  image in Case 1: sparse stripes. (a) Original. (b) Degraded. (c) WFAF. (d) ASSTV. (e) LRID. (f) LRTD. (g) LLRGTV. (h) NMoG. (i) LRHP.

still low-contrast stripes on the simulated image as in Fig. 5(a). Compared with LRHP, the results of other approaches, which cannot eliminate the weak, are closer to the original image. On the other hand, the HP decomposition item is enforced on every band. If stripes of the experimental data were not across all the bands, LRHP failed to preserve the information from the clean observations as greatly as NMoG. This is also where LRHP needs to be improved.

In Case 2, because of the existence of complex and dense stripes, the indicators of all methods dropped compared to Case 1. In addition, ASSTV, LRID, LRTD, LLRGTV, and

NMoG require more time to reach convergence. The superiority of LRHP is evident in Case 2 with regard to desstriping performance and computational costs. This is because the HSI component and stripe component are treated equally in the LRHP model work, thereby benefiting the iterative estimation process. Moreover, notably lower high-order metrics (absolute values of skewness and kurtosis) further validate LRHP's ability to handle stripes with various intensities.

2) *Visual Quality Comparison*: Figs. 5–7 show the visual results of different desstriping methods. As shown in Fig. 5, partial stripes are not removed in WFAF, and the artifact

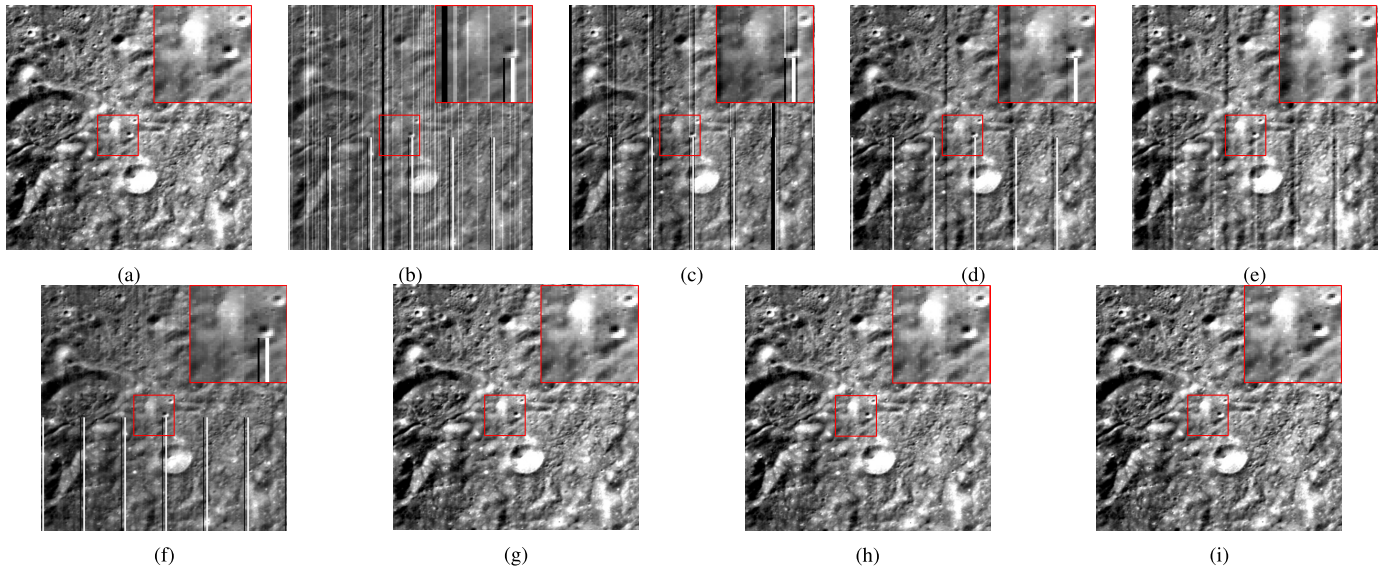


Fig. 6. Destriping results for simulated M<sup>3</sup> image in Case 2: dense stripes (band 24). (a) Original. (b) Degraded. (c) WFAF. (d) ASSTV. (e) LRID. (f) LRTD. (g) LLRGTV. (h) NMoG. (i) LRHP.

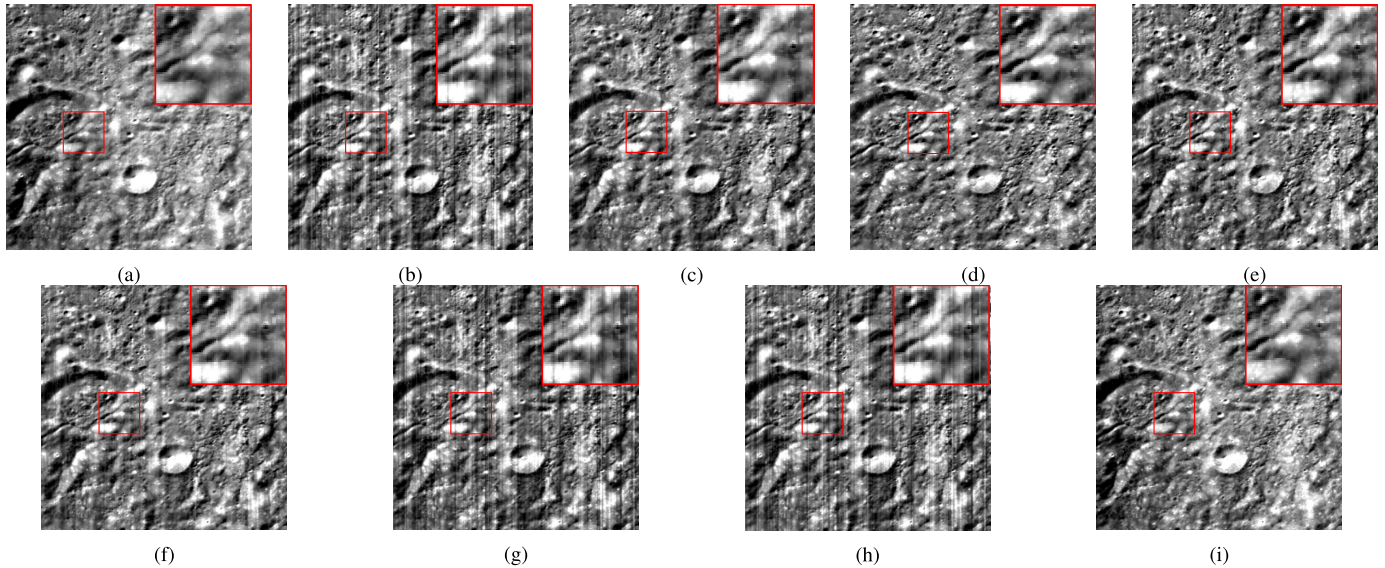


Fig. 7. Destriping results for simulated M<sup>3</sup> image in Case 2: dense stripes (band 33). (a) Original. (b) Degraded. (c) WFAF. (d) ASSTV. (e) LRID. (f) LRTD. (g) LLRGTV. (h) NMoG. (i) LRHP.

appears at the position of the thick stripe. ASSTV and LRID can eliminate most stripes but the artifacts caused by the thick stripe still exist and LRTD is not effective for partial stripes. LLRGTV, NMoG, and LRHP remove all types of stripes completely, and their visual results are comparable.

In Case 2, the global, partial stripes, periodic, and non-periodic stripes are all contained in band 24 [see Fig. 6(b)]. It can be observed that WFAF fails to remove stripes, and ASSTV, LRID, and LRTD cannot obtain good results due to the existence of partial stripes. LLRGTV, NMoG, and LRHP still achieve a generally good visual level, but LLRGTV and NMoG miss some weak stripes as displayed in the enlarged region in the red box. The periodic, nonperiodic, homogeneous, heterogeneous, and thick stripes are contained in band 33. Fig. 7(g) and (h) shows that LLRGTV and

NMoG fail to remove most of the stripes. WFAF, ASSTV, LRID, and LRTD eliminate most of the stripes successfully, but slight artifacts and the spectral distortion make their performance imperfect. LRHP obtains the best visual quality by removing all the stripes and maintaining details and spectral information.

#### D. Real Experiments

To verify the robustness of the proposed LRHP in different areas, we selected M<sup>3</sup> images of three typical regions to further test performance.

- 1) *Region 1 (Finsen Crater)*: Finsen Crater situates on the northeast side of the Von Kármán Crater (the landing site of Chang'E-4), within the South Pole-Aitken basin

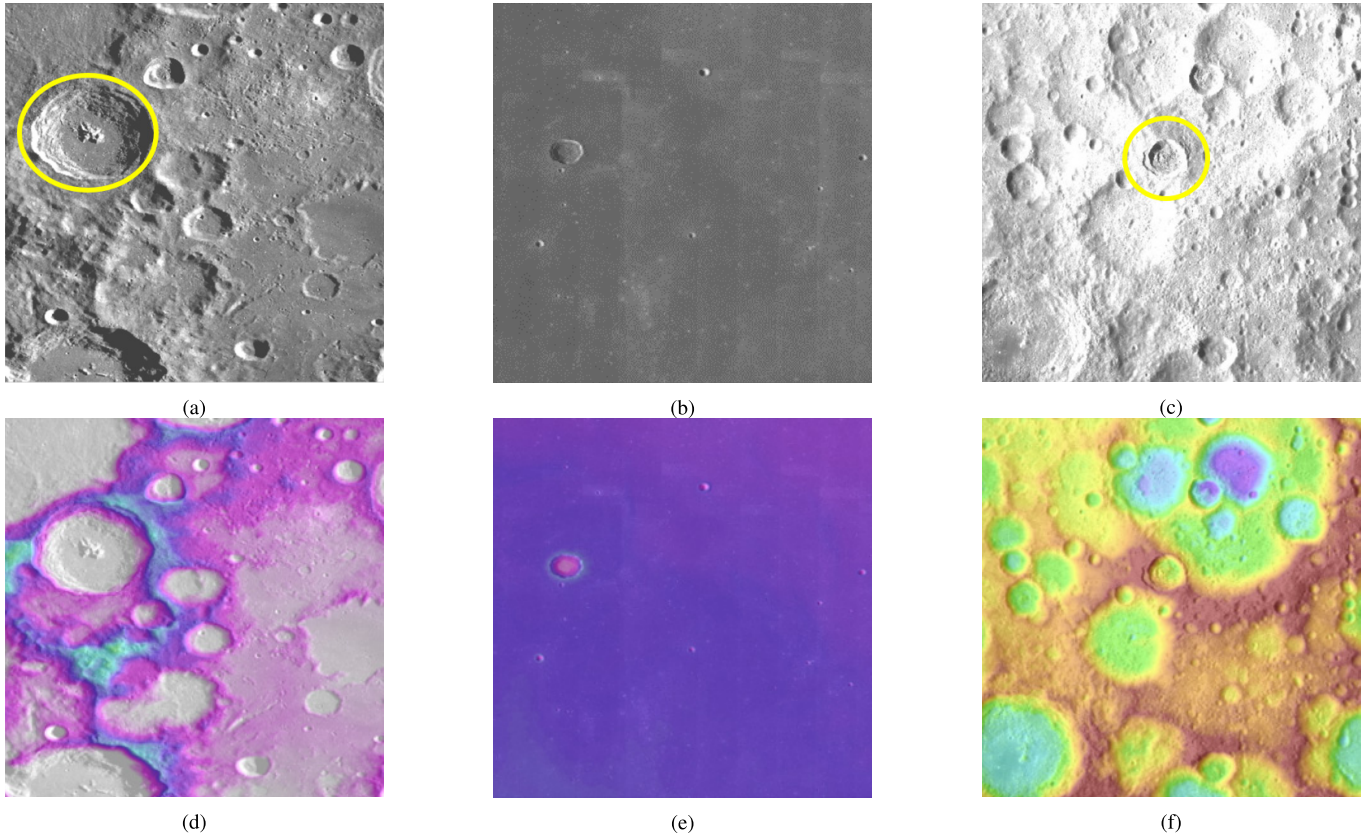


Fig. 8. Three typical research regions. (a) Finsen Crater. (b) Mare Iridum. (c) Necho Crater. (d) Terrain of (a). (e) Terrain of (b). (f) Terrain of (c). The first line is based on the global morphologic map obtained by the Lunar Reconnaissance Orbiter (LRO) Wide Angle Camera (WAC) [61], and the second line is based on the topography map acquired by the Lunar Orbiter Laser Altimeter (LOLA) instrument [62].

of the Moon's far side [63]. Finsen is a relatively young impact crater with well-defined features that have not been significantly eroded by subsequent impacts [see Fig. 8(a)] [64], [65].

- 2) *Region 2 (Mare Imbrium)*: Mare Imbrium is a vast lava plain within the Imbrium Basin with less distinctive features than other areas of the Moon as shown in Fig. 8(b) and (e) because molten lava pooled in the craters and formed a relatively smooth surface [66].
- 3) *Region 3 (Necho Crater)*: Necho crater lies on the far side of the Moon, too, and it is surrounded by various sizes of impact craters [see Fig. 8(c)]. The most distinctive aspect of this crater is the prominent ray system that surrounds the outer rim (see Fig. 11) [67].

Given that there are almost no stripe-free regions in all the bands, only one nonreference index, the mean inverse coefficient of variation (MICV) [68] was adopted to assess the destriping performance in the real data experiments. The definition of MICV is

$$\text{MICV} = \frac{1}{B} \sum_{i=1}^B \frac{R_{m_i}}{R_{s_i}} \quad (28)$$

where  $R_{m_i}$  and  $R_{s_i}$  denote the mean and standard deviation of a selected datacube region's  $i$ th band, respectively. We randomly selected three  $10 \times 10$  regions on the three images to calculate their MICVs. The higher the MICV, the lower the

level of stripe noises contained in the restoration result with the higher quality destriping performance.

The quantitative indicators are presented in Table II. LRHP obtains the highest MICVs in all the samples on three regions; thereby illuminating how LRHP outperforms the other compared algorithms. In addition, LRHP is efficient and stable in different areas according to the running time.

Figs. 9–11 show the results of various destriping techniques for Finsen Crater, Mare Imbrium, and Necho Crater. LRHP successfully suppresses all the stripes in various images and preserves underlying image structures, as shown in Figs. 9–11(h). ASSTV also performs well, but the results of ASSTV are a bit oversmooth. The enlarged region in Fig. 10 is the protruding Imbrium Sculpture, but ASSTV weakens this feature compared to LRHP. In addition, the local spectral distortion of ASSTV is more obvious than the other methods as shown in the enlarged region of Fig. 11. WFAF, LRID, LRTD, LLRGTV, and NMoG cannot remove stripes thoroughly, therefore, there are stripe noises remained and artifacts occurred in some cases.

Fig. 12 shows the mean cross-track profiles from the experiments on the three regions. In the images destriped with LRHP, most of the fluctuations in the original degraded images are reduced while maintaining the original mean digital numbers (DNs). Although ASSTV also smoothes the fluctuations to a certain extent, it causes a relatively large change in the mean DNs, which can explain the local oversmoothing and

TABLE II  
PERFORMANCE COMPARISON OF REAL EXPERIMENTS ON ALL COMPETING METHODS

Region 1: Finsen Crater							
Index	WFAF	ASSTV	LRID	LRTD	LLRGTV	NMoG	LRHP
MICV1	32.4521	37.6092	36.7921	<u>39.2610</u>	39.0136	37.5551	<b>41.8514</b>
MICV2	24.8296	26.6655	25.9088	<u>27.7314</u>	26.6125	26.5112	<b>29.5658</b>
MICV3	39.7882	<u>42.7409</u>	39.8810	40.2483	38.0417	37.5875	<b>51.4119</b>
Time/s	<b>5.10</b>	85.51	856.63	161.58	285.36	292.75	<u>15.94</u>
Region 2: Mare Iridum							
Index	WFAF	ASSTV	LRID	LRTD	LLRGTV	NMoG	LRHP
MICV1	4.9079	<u>5.0872</u>	4.7896	5.0527	4.9391	4.9153	<b>5.8256</b>
MICV2	19.8036	21.2490	20.8574	<u>21.8267</u>	19.5975	19.0976	<b>25.0767</b>
MICV3	6.8169	<u>7.2987</u>	6.7044	7.0048	6.7161	6.7094	<b>7.2987</b>
Time/s	<b>4.37</b>	73.25	733.85	138.42	244.46	250.79	<u>16.08</u>
Region 3: Necho Crater							
Index	WFAF	ASSTV	LRID	LRTD	LLRGTV	NMoG	LRHP
MICV1	46.0617	<u>52.5810</u>	51.0708	39.9488	39.1857	38.0078	<b>61.7865</b>
MICV2	37.9788	43.8196	<u>44.2802</u>	40.7119	39.1092	35.4736	<b>46.6028</b>
MICV3	35.2409	<u>41.0568</u>	41.0477	37.4851	35.6455	35.4736	<b>42.5602</b>
Time/s	<b>4.48</b>	73.30	724.58	137.5194	352.5484	202.1896	<u>16.81</u>

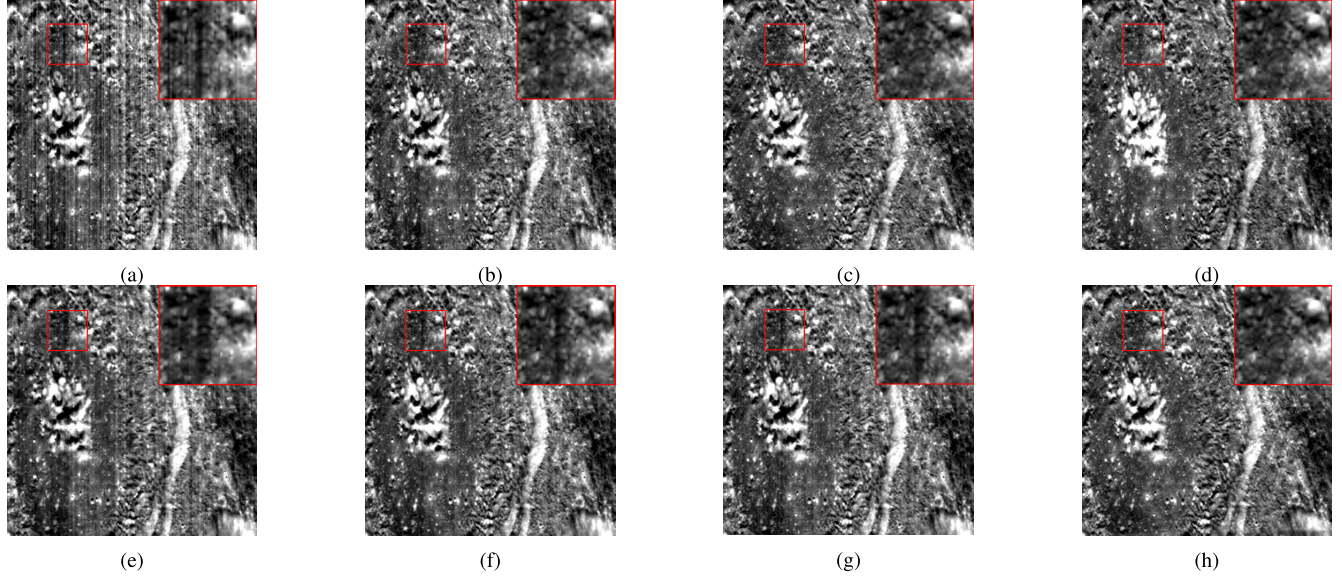


Fig. 9. Destriping results for real M<sup>3</sup> image in Finsen Crater: band 15. (a) Original. (b) WFAF. (c) ASSTV. (d) LRID. (e) LRTD. (f) LLRGTV. (g) NMoG. (h) LRHP.

spectral distortion in the visual results of ASSTV. The other compared methods smooth a few fluctuations while preserving the original mean DN level, but they cannot remove all the stripe noise.

Fig. 13 shows the spectral signatures of pixel (250, 150) of both the original data and destriped results. It can be found that WFAF, LRTD, LLRGTV, NMoG, and LRHP have high spectral fidelity; there, LRTD and LRHP retain the most spectral information. LRID and ASSTV have a marginally great spectral distortion before 1000 nm and after 2000 nm because the corruption in these bands is more serious.

Consequently, the proposed LRHP outperforms the other prevalent destriping methods quantitatively and visually in

the experiments with M<sup>3</sup> images. Furthermore, the experimental results show that LRHP can maintain the spectral information, which benefits the following interpretations and applications. In Section IV-B, we will further explore whether LRHP can facilitate the subsequent analysis by utilizing the IBD [69], [70] mapping.

#### E. Sensitivity Analysis of Parameters

There are four important parameters in the proposed LRHP:  $\lambda_1$ ,  $\lambda_2$ ,  $\beta$ , and  $\lambda_{gp}$ . Since the specific noise levels and percentages of stripes vary in different M<sup>3</sup> images, the corresponding regularization parameters in LRHP need to be tuned according

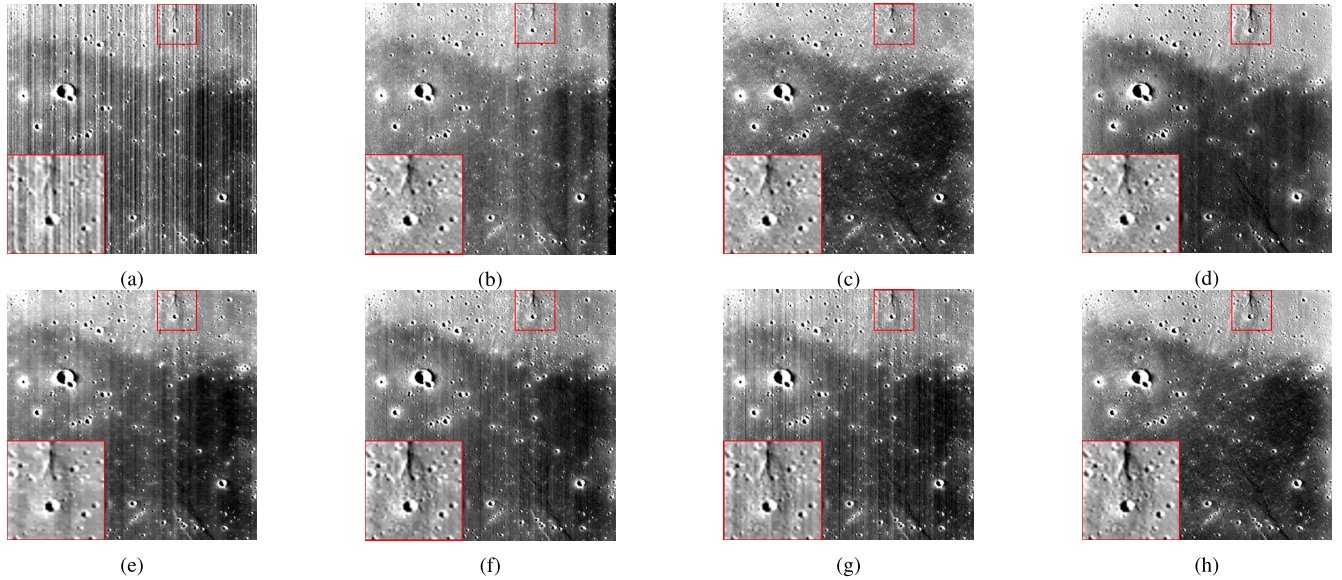


Fig. 10. Destriping results for real  $M^3$  image in Mare Iridum: band 15. (a) Original. (b) WFAF. (c) ASSTV. (d) LRID. (e) LRTD. (f) LLRGTV. (g) NMoG. (h) LRHP.

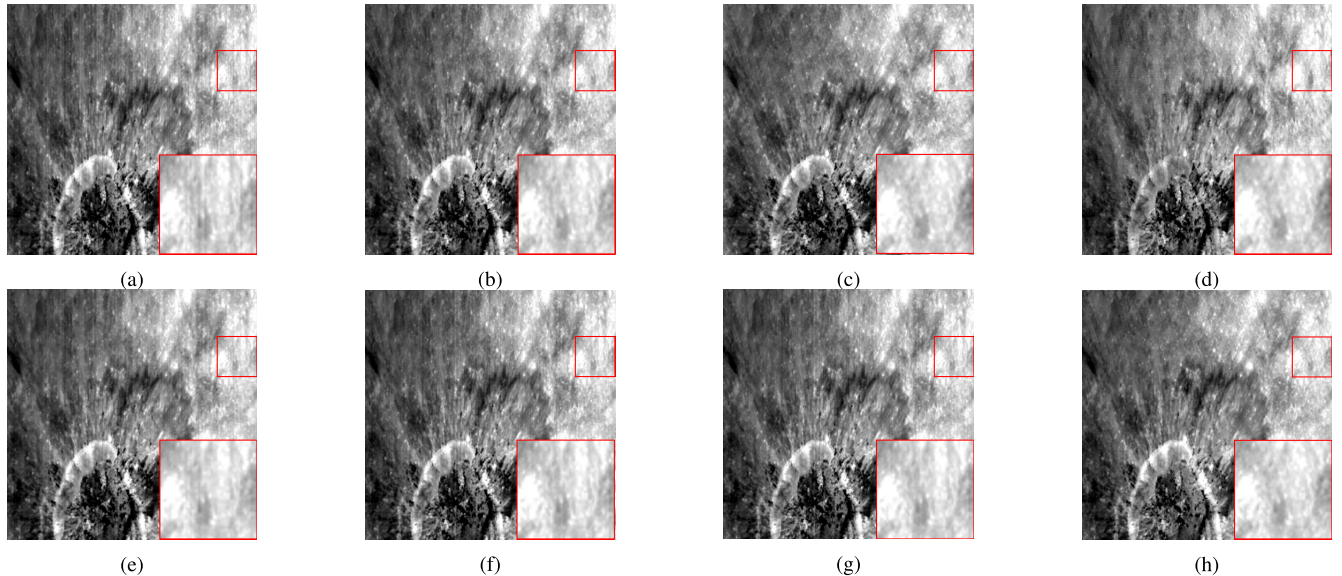


Fig. 11. Destriping results for real  $M^3$  image in Necho Crater: band 75. (a) Original. (b) WFAF. (c) ASSTV. (d) LRID. (e) LRTD. (f) LLRGTV. (g) NMoG. (h) LRHP.

to the degradation levels. To clarify the sensitivity analyses of these parameters, we select two different stripe degradation levels from the simulated data experiments as examples, i.e., sparse stripes and dense stripes, respectively. The MPSNR and MSSIM are employed as the criterion to evaluate the selection of parameters.

1) *Sensitivity Analysis of  $\lambda_1$ :* In the LRHP solver,  $\lambda_1$  is used to balance the contributions of the low-rank enforced HSI component and the data-fidelity item guided by the HP decomposition. By varying  $\lambda_1$  in the set of 0.001, 0.01, 0.1, 1, 10, 100, 100, the destriping results in terms of MPSNR and MSSIM metrics are shown in Fig. 14(a) and (e). As can be observed, the performance of the proposed LRHP is best when  $\lambda_1 = 0.01$  in the case of sparse stripes. When the stripes are dense,  $\lambda_1$  should be in [5,10] to achieve the best results.

2) *Sensitivity Analysis of  $\lambda_2$ :*  $\lambda_2$  restricts the rank of the stripe component. Fig. 14(b) and (f) shows the MPSNR and MSSIM values of the LRHP solver with different  $\lambda_2$  values in two cases. When the stripes are sparse,  $\lambda_2$  greater than 0.01 can lead to a stable result, while densely distributed stripes demand  $\lambda_2$  greater than 1.

3) *Sensitivity Analysis of  $\beta$ :*  $\beta$  tradeoffs the contributions between the data-fidelity item and other items. Fig. 14(c) and (g) shows the experimental results of MPSNR and MSSIM versus  $\beta$  under different degradation levels. It can be observed that the results are optimal when  $\beta = 0.01$  regardless of the stripe level.

4) *Sensitivity Analysis of  $\lambda_{gp}$ :* In the proposed LRHP model,  $\lambda_{gp}$  is used to control the smoothness of the mean cross-track profiles. As can be seen in Fig. 14(d) and (h), better results

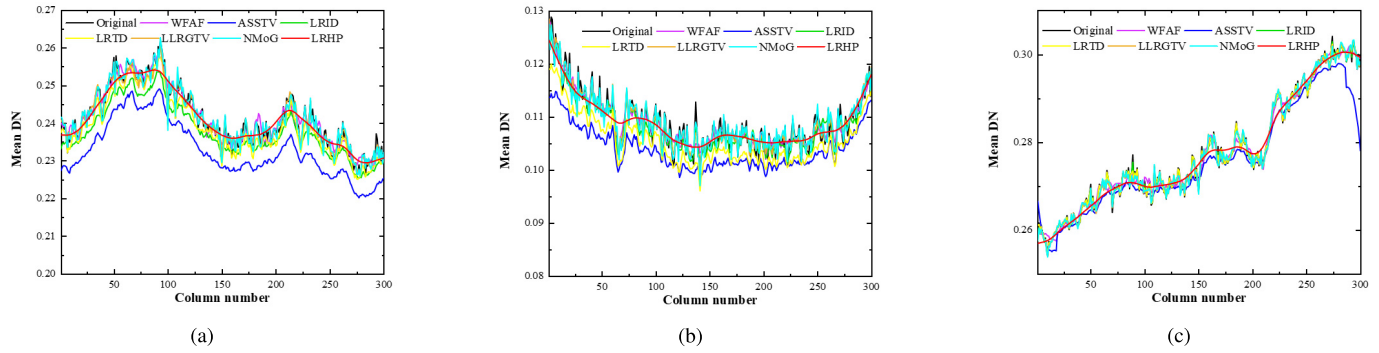


Fig. 12. Mean cross-track profiles for real experimental results. (a) Finsen Crater: band 15. (b) Mare Iridum: band 15. (c) Necho Crater: band 75.

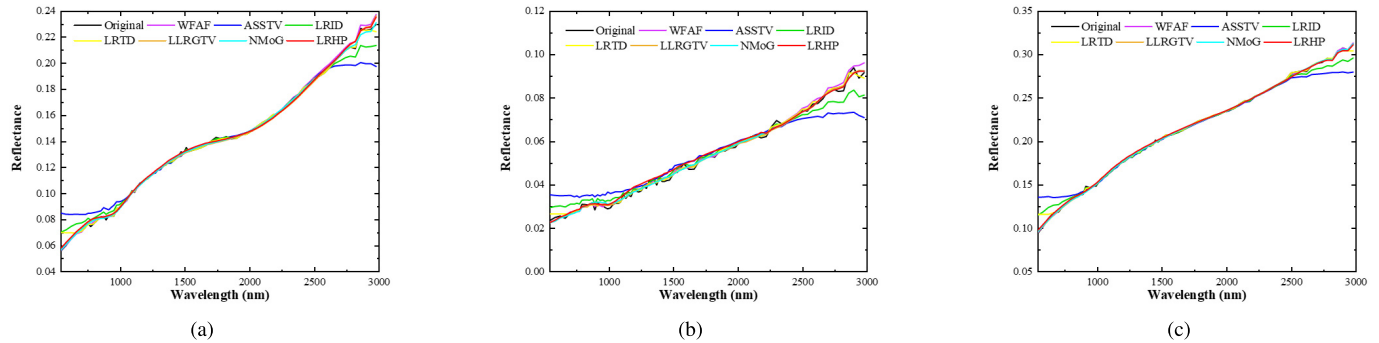


Fig. 13. Reflectance of pixel (250, 150). (a) Finsen Crater. (b) Mare Iridum. (c) Necho Crater.

stem from greater  $\lambda_{gp}$ . However, the performance is best when  $\lambda_{gp}$  in both cases, and thus, the selection of  $\lambda_{gp}$  is relatively independent of the noise level.

Overall, the parameter setting of LRHP is relatively stable because half of the parameters are fixed:  $\beta = 0.01$  and  $\lambda_{gp} = 100$ . Furthermore, we recommend  $\lambda_1 = 0.01$  and  $\lambda_2 = 0.01$  for destriping less-striped M<sup>3</sup> images obtained in the early stage of its mission. When the stripes become dense,  $\lambda_1 = 5$  and  $\lambda_2 = 5$  will fit better.

## IV. DISCUSSION

In Section IV-B, the generalization ability of the proposed LRHP is explored through experiments on another lunar HSI data set and commonly used terrestrial remote sensing images. Also, a spectral analysis before and after destriping is presented in the second section.

### A. Generalization on Other Data Sets

To test the generalization of the proposed LRHP, the interference imaging spectrometer (IIM) data obtained by Chang'E-1 and four widely used terrestrial remote sensing images that are corrupted by stripes: Hyperion, Aqua MODIS, GaoFen-5 [71], and OrbitaHyperSpectral-1(OHS-1) are selected as experimental data for further validation.

During the experiments, we follow the principles of parameter selection mentioned in Section III-E. For IIM, Aqua MODIS, and OHS-1, parameters are set as the case of dense stripes, whereas the parameters of Hyperion and GaoFen-5 are adjusted as the case of sparse stripes.

*1) Experiments on Other Lunar HSIs:* M<sup>3</sup> and IIM are the only two HSI data sets of the Moon. IIM is loaded on Chang'E-1, which was launched in 2007 [72]. The 32-band IIM data are obtained by push-room imaging from 480 to 960 nm. Its spatial resolution is 200 m/pixel and it covers 78% of the lunar surface [73]–[75]. Unlike M<sup>3</sup>, IIM is not only corrupted by stripes but also affected by nonindependent and identically (non-i.i.d.) distributed noises. To test the generalization ability of LRHP, IIM data were recovered by LRHP and other compared algorithms, the quantitative indices are listed in Table III, and the visual results are shown in Fig. 15.

From the indicators in Table III, it can be observed that the proposed LRHP is superior to other competing approaches in terms of MICV values, and LRHP is the second-fastest method only after WFAF. Meanwhile, based on the visual results and local enlarged regions, we can find that WFAF can recognize and remove stripe noises accurately, but eliminating other types of noises is beyond its capability. In the case of mixed noise interference, ASSTV and LRID have marginally more residue. In addition to LRHP, LRTD, LLRGTV, and NMoG also successfully removed most of the noise, but there are still weak stripe residues. Overall, LRHP achieved the best results in a relatively short time among all the competing methods even in the case of mixed noise. Accordingly, it can also be applied to improve the quality of Chang'E-1 IIM data set perfectly.

2) *Experiments on Terrestrial Remote Sensing Images:*  
 Similarly, terrestrial remote sensing images are also degraded by noise because of the limitations of sensor manufacturing

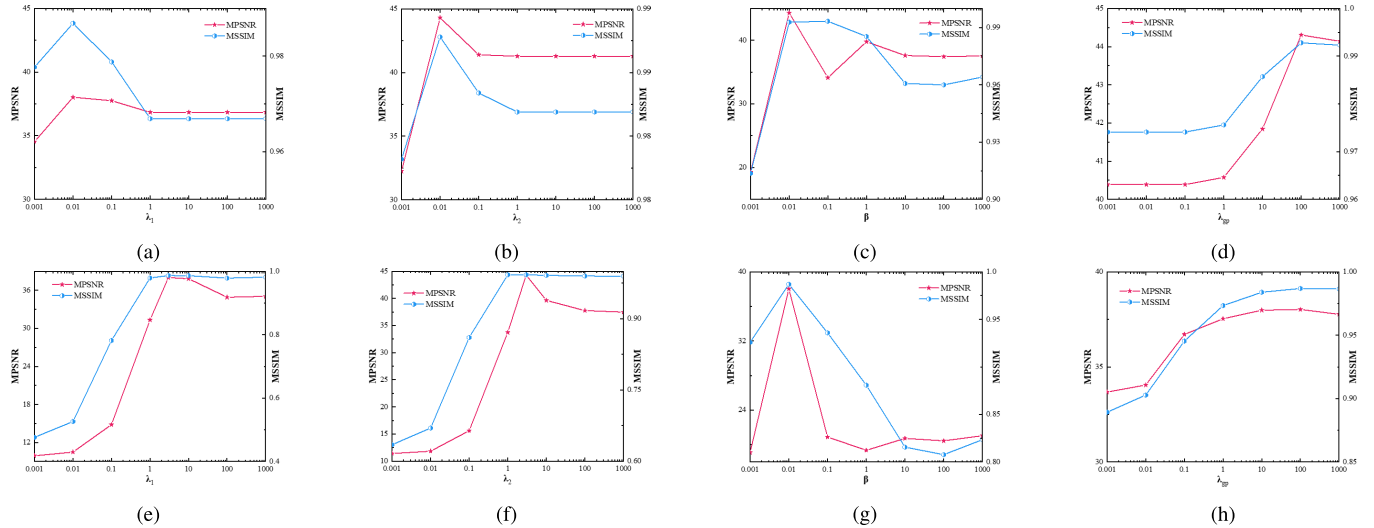
Fig. 14. Sensitivity analysis of parameters. Case 1: (a)  $\lambda_1$ , (b)  $\lambda_2$ , (c)  $\beta$ , and (d)  $\lambda_{\text{gp}}$ . Case 2: (e)  $\lambda_1$ , (f)  $\lambda_2$ , (g)  $\beta$ , and (h)  $\lambda_{\text{gp}}$ .

TABLE III  
PERFORMANCE COMPARISON OF EXPERIMENTS OF IIM DATA ON ALL COMPETING METHODS

Index	WFAF	ASSTV	LRID	LRTD	LLRGTV	NMoG	LRHP
MICV1	7.4913	7.8339	7.9001	8.7471	9.0556	<u>9.1090</u>	<b>14.2088</b>
MICV2	9.9467	9.5768	9.9580	11.6163	12.4108	<u>12.4796</u>	<b>21.0835</b>
MICV3	4.3444	4.3114	4.3754	4.3050	<u>4.3743</u>	4.3373	<b>7.8609</b>
Time/s	<b>0.33</b>	22.70	61.49	19.279	13.54	14.19	<u>3.08</u>

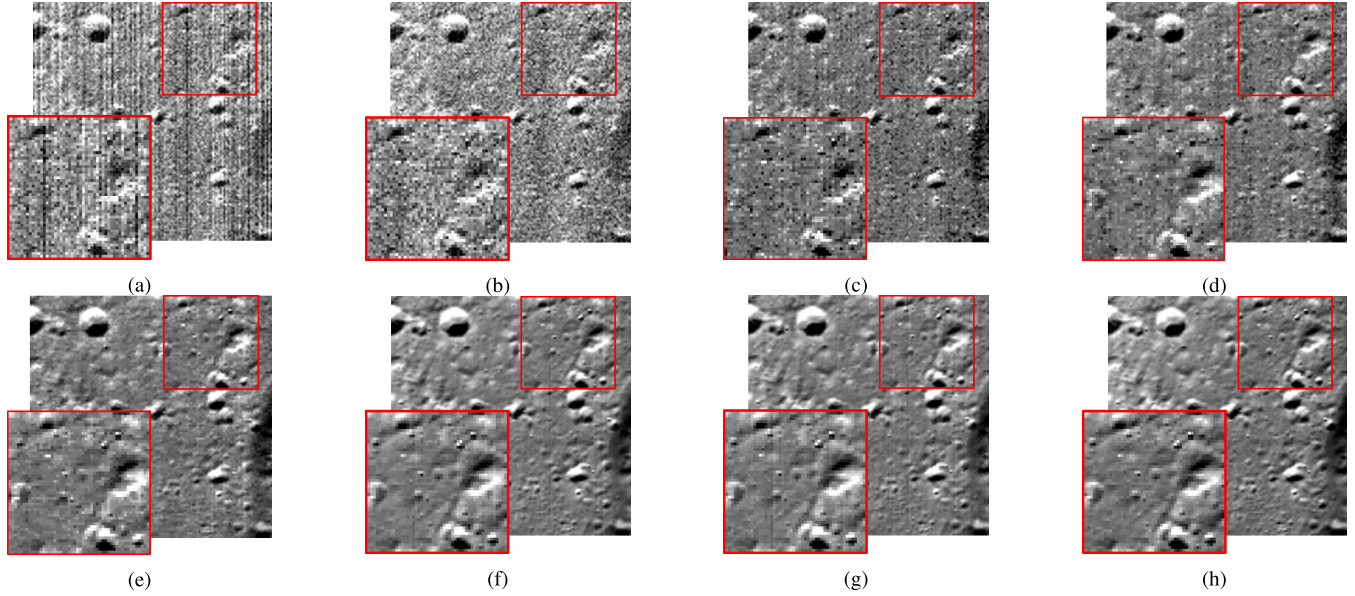


Fig. 15. Destriping results of IIM data set. (a) IIM: band 3. (b) WFAF. (c) ASSTV. (d) LRID. (e) LRTD. (f) LLRGTV. (g) NMoG. (h) LRHP.

technology and environmental impact. Hyperion and GaoFen-5 are contaminated by low-level stripes and Gaussian noise, Aqua MODIS is affected by periodic but thick stripes, and OHS-1 is corrupted by severe nonperiodic stripes and Gaussian noise.

Through the restoration results shown in Fig. 16, we can find that LRHP can achieve stable recovery results for both the multispectral image (MSI), which is corrupted by dense stripes [see Fig. 16(b)], and the HSIs with mixed noises [see Fig. 16(a), (c), and (d)]. Albeit LRHP is designed for  $M^3$

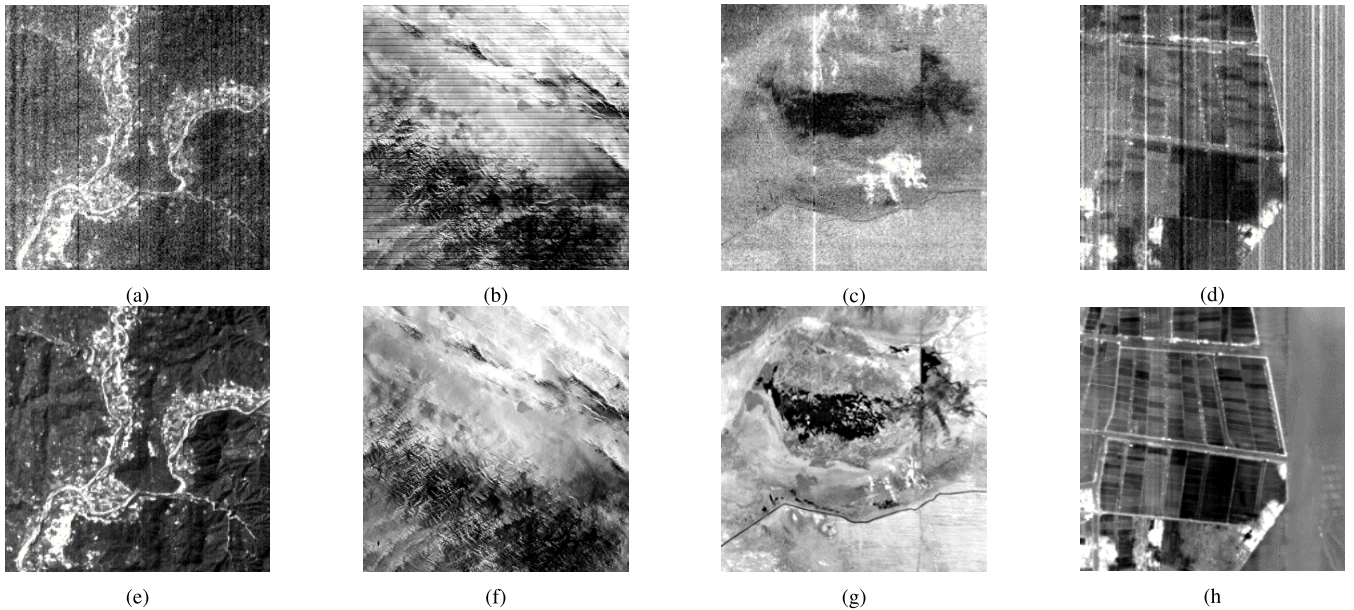


Fig. 16. Destriping results of commonly used terrestrial data sets. (a) Hyperion: band 1. (b) Aqua MODIS: band 30. (c) GaoFen-5: band 193. (d) OHS-1: band 14. (e) Hyperion: LRHP. (f) Aqua MODIS: LRHP. (g) GaoFen-5: LRHP. (h) OHS-1: LRHP.

data, its flexible model can be applied to different image data sets, too. The low-rank constraints enforced on the image component can remove the mixed noises effectively. Meanwhile, the HP decomposition guidance and low-rank prior to the stripe component on every single band contribute to the good results on MSIs with fewer bands. To sum up, the proposed LRHP has great generalization performance on commonly used terrestrial remote sensing data sets.

#### B. Spectral Analysis via IBD Mapping

IBDs is a widely used spectral parameter for studies of M<sup>3</sup> [69], [70], [76]: the absorption depths of all the bands are summed in a certain range around the absorption peak, thereby reflecting the absorption peak depth of minerals. Therefore, combining the IBD parameters of several characteristic absorption peaks into a false-color map can help us identify the distribution of certain important minerals. Three types of IBD parameters are employed in our work: IBD1000, IBD2000, and IBD1508, therein, IBD1508 is the reflectance at 1508 nm and the definitions of the other parameters are as follows:

$$\text{IBD1000} = \sum_{n=0}^{26} \left( 1 - \frac{R(789 + 20n)}{R_c(789 + 20n)} \right) \quad (29)$$

$$\text{IBD2000} = \sum_{n=0}^{21} \left( 1 - \frac{R(1658 + 40n)}{R_c(1658 + 40n)} \right) \quad (30)$$

where  $R$  denotes the reflectance at a given wavelength and  $R_c$  is the continuum removed reflectance. The continuum removed reflectance is obtained by removing a linear continuum using the reflectance at 750, 1578, and 2000 nm from the original spectral signature. In this way, the spectral red shift can be removed, and the spatial weathering effect can

be minimized, thereby making the absorption peaks presented more clearly [77].

After generating the IBD maps of the three regions, the image of Finsen is taken as an example and extracted from the spectra of yellow, orange, and blue regions, respectively. Combining the IBD maps in Fig. 17 and the spectral signatures in Fig. 18, it can be observed that the #1 spectra extracted from the yellow region have strong mafic absorptions, and obvious absorption peaks around 1000 and 2000 nm, thereby representing pyroxene minerals. The #2 spectra extracted from the blue region is relatively smooth without obvious absorption characteristics. Meanwhile, considering that the blue area is widely distributed, it can be inferred as plagioclase or crystalline plagioclase. As for #3 spectra from the orange area, their absorption features are similar with #1 spectra after continuum removing, but their absorption peaks are wider than those of #1 at 1000 nm as shown in Fig. 18(b); hence, they denote olivine.

The texture features of Finsen Crater are the most abundant, as shown in Fig. 17(a) and (d). Pyroxene distributes in its center densely, and the presence of olivine can be seen. Similarly, olivine can also be found in Necho Crater, as shown in Fig. 17(c) and (f). This shows that the mineral distributions of Finsen and Necho are in accord with the magma ocean theory. In addition, Necho has a distinguished prominent ray system, and the highly asymmetric sputter deposition surrounds it. Pyroxene distributes inside Necho in a ring shape, and a large amount of pyroxene also exists outside the northeast part of the crater, too, thereby indicating that the impact of this site is violent.

Comparing the IBD maps before and after destriping in Fig. 17, it can be found that although IBD mapping has been able to slightly reduce the effect of stripe noises, the spectral parameter maps are still improved obviously after destriping,

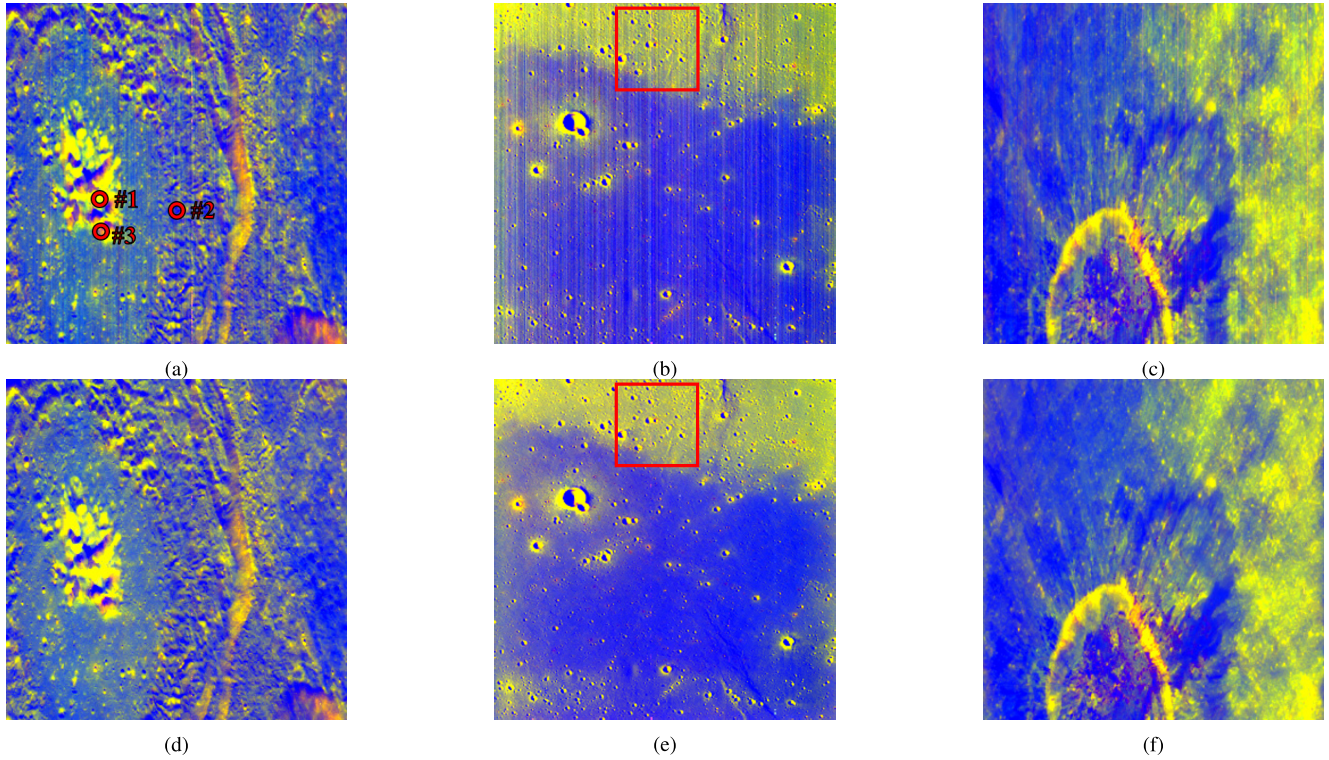


Fig. 17. IBD false-color maps. (a) Finsen Crater: Original. (b) Mare Iridum: Original. (c) Necho Crater: Original. (d) Finsen Crater: LRHP. (e) Mare Iridum: LRHP. (f) Necho Crater: LRHP. (R: IBD1000; G: IBD2000; B: IBD 1508 nm reflectance. The concentric circles in (a) are the three sampling points for the spectral analysis.)

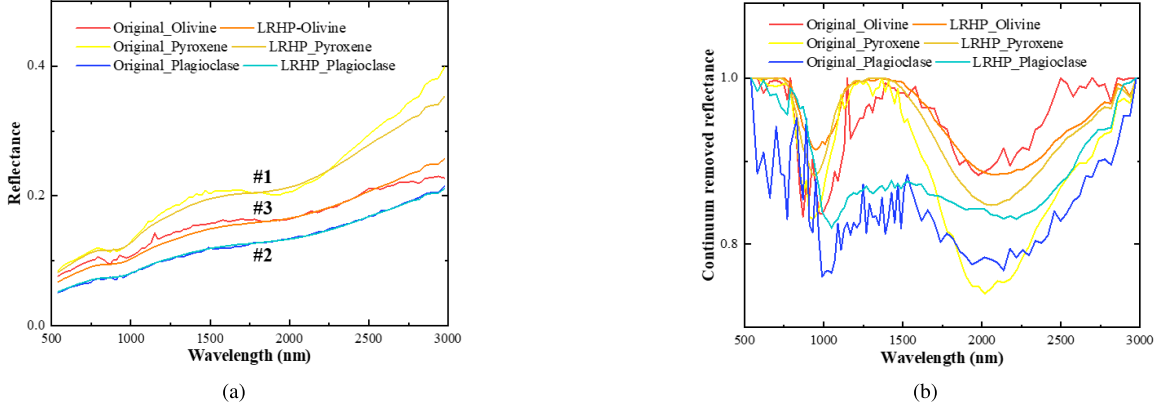


Fig. 18. Spectral analysis. (a) Original spectra. (b) Continuum removed spectra.

especially for research areas heavily corrupted by stripes, such as Mare Imbrium. For instance, the presence of stripes makes the pyroxene sample in the red box of Fig. 17(b) misidentified as a mixture of small proportions of pyroxene and large proportions of olivine. After destriping, the error of spectral analysis is eliminated. As for regions that are less contaminated, such as Finsen and Necho, the stripe noises affect the overall mineral distribution analysis less, but they still harm the subsequent content extraction of minerals or specific elements. After destriping, these interferences are also effectively removed, and the overall distribution and local details are preserved as displayed in the second line of Fig. 17.

Therefore, LRHP not only improves the spatial quality of M<sup>3</sup> but also largely maintains the original spectral information,

which can facilitate subsequent applications (such as retrieving the distribution and content of surface materials, fine-scaled analysis by fusing with high-resolution panchromatic images, and so on).

## V. CONCLUSION AND FUTURE WORK

In this article, we have proposed a fast and effective destriping method for M<sup>3</sup> hyperspectral imagery. Considering that the intensities and locations of stripes in different bands are different, and several bands are too degraded to provide effective information for the optimization procedure, the HP decomposition is applied to estimate the desired mean cross-track profile, thereby offering reference distribution information to the following steps. Then, it is combined with the low-rank

prior to constrain the HSI together. Meanwhile, the low-rank constraint is also enforced on the stripes and equally treated with the image to reduce the loss of details and accelerate the convergence.

The experiments are performed on both the simulated and real M<sup>3</sup> images. The results verify that the proposed LRHP achieves superiority over other state-of-the-art methods. The rapidity and accuracy of LRHP make it more suitable for M<sup>3</sup> data set that contains enormous images. The expanding experiments on the IIM data set and commonly used terrestrial remote sensing images demonstrate that LRHP has good generalization ability. Besides, the IBD maps illustrate that LRHP can maintain the original clean observation well while restoring, which is of great significance for subsequent exploration and analysis of Moon, which is of great significance for subsequent exploration and analysis of Moon.

Nevertheless, the parameters of this algorithm need to be adjusted manually according to the noise level of images. Therefore, we will explore how to evaluate the noise level of the image automatically, thereby making the parameter adaptive in the future.

#### ACKNOWLEDGMENT

The authors would like to thank the editor, associated editor, and anonymous reviewers for their helpful comments and suggestions to improve this article, and the science teams of M<sup>3</sup>, Chang'E-1, Hyperion, Aqua Moderate Resolution Imaging Spectroradiometer (MODIS), GaoFen-5, and OrbitaHyperSpectral-1 (OHS-1) for offering numerous research data. They would also like to thank all the researchers for offering the codes of the algorithms used for comparison in experiments.

#### REFERENCES

- [1] Y. Zheng, Z. Ouyang, C. Li, J. Liu, and Y. Zou, "China's lunar exploration program: Present and future," *Planet. Space Sci.*, vol. 56, no. 7, pp. 881–886, May 2008.
- [2] N. Acito, M. Diani, and G. Corsini, "Subspace-based striping noise reduction in hyperspectral images," *IEEE Trans. Geosci. Remote Sens.*, vol. 49, no. 4, pp. 1325–1342, Apr. 2011.
- [3] K. Tan, F. Wu, Q. Du, P. Du, and Y. Chen, "A parallel Gaussian–Bernoulli restricted Boltzmann machine for mining area classification with hyperspectral imagery," *IEEE J. Sel. Topics Appl. Earth Observ. Remote Sens.*, vol. 12, no. 2, pp. 627–636, Feb. 2019.
- [4] H. Carfantan and J. Idier, "Statistical linear destriping of satellite-based pushbroom-type images," *IEEE Trans. Geosci. Remote Sens.*, vol. 48, no. 4, pp. 1860–1871, Apr. 2010.
- [5] R. Pande-Chhetri and A. Abd-Elrahman, "De-striping hyperspectral imagery using wavelet transform and adaptive frequency domain filtering," *ISPRS J. Photogramm. Remote Sens.*, vol. 66, no. 5, pp. 620–636, Sep. 2011.
- [6] J. Jia *et al.*, "Destriping algorithms based on statistics and spatial filtering for visible-to-thermal infrared pushbroom hyperspectral imagery," *IEEE Trans. Geosci. Remote Sens.*, vol. 57, no. 6, pp. 4077–4091, Jun. 2019.
- [7] X. Liu, H. Shen, Q. Yuan, X. Lu, and C. Zhou, "A universal destriping framework combining 1-D and 2-D variational optimization methods," *IEEE Trans. Geosci. Remote Sens.*, vol. 56, no. 2, pp. 808–822, Feb. 2018.
- [8] Q. Zhang, Q. Yuan, J. Li, F. Sun, and L. Zhang, "Deep spatio-spectral Bayesian posterior for hyperspectral image non-i.i.d. Noise removal," *ISPRS J. Photogramm. Remote Sens.*, vol. 164, pp. 125–137, Jun. 2020.
- [9] C. M. Pieters *et al.*, "The moon mineralogy mapper (m<sup>3</sup>) on Chandrayaan-1," *Curr. Sci.*, pp. 500–505, Feb. 2009.
- [10] R. Green *et al.*, "The moon mineralogy mapper (M<sup>3</sup>) imaging spectrometer for lunar science: Instrument description, calibration, on-orbit measurements, science data calibration and on-orbit validation," *J. Geophys. Res. Planets*, vol. 116, no. E10, Oct. 2011, Art. no. E00G19.
- [11] Y. Zhong, W. Li, X. Wang, S. Jin, and L. Zhang, "Satellite-ground integrated destriping network: A new perspective for EO-1 hyperion and Chinese hyperspectral satellite datasets," *Remote Sens. Environ.*, vol. 237, Feb. 2020, Art. no. 111416.
- [12] J.-J. Pan and C.-I. Chang, "Destriping of landsat MSS images by filtering techniques," *Photogramm. Eng. Remote Sens.*, vol. 58, p. 1417, Jan. 1992.
- [13] J. J. Simpson, J. R. Stitt, and D. M. Leath, "Improved finite impulse response filters for enhanced destriping of geostationary satellite data," *Remote Sens. Environ.*, vol. 66, no. 3, pp. 235–249, Dec. 1998.
- [14] J. Simpson, "Improved destriping of GOES images using finite impulse response filters," *Remote Sens. Environ.*, vol. 52, no. 1, pp. 15–35, Apr. 1995.
- [15] J. Chen, Y. Shao, H. Guo, W. Wang, and B. Zhu, "Destriping MODIS data by power filtering," *IEEE Trans. Geosci. Remote Sens.*, vol. 41, no. 9, pp. 2119–2124, Sep. 2003.
- [16] J. Torres and S. O. Infante, "Wavelet analysis for the elimination of striping noise in satellite images," *Opt. Eng.*, vol. 40, pp. 1309–1314, Jul. 2001.
- [17] J. Chen, H. Lin, Y. Shao, and L. Yang, "Oblique striping removal in remote sensing imagery based on wavelet transform," *Int. J. Remote Sens.*, vol. 27, no. 8, pp. 1717–1723, Feb. 2007.
- [18] B. Münch, P. Trtik, F. Marone, and M. Stampanoni, "Stripe and ring artifact removal with combined wavelet–Fourier filtering," *Opt. Exp.*, vol. 17, no. 10, pp. 8567–8591, Jun. 2009.
- [19] B. K. P. Horn and R. J. Woodham, "Destriping LANDSAT MSS images by histogram modification," *Comput. Graph. Image Process.*, vol. 10, no. 1, pp. 69–83, May 1979.
- [20] J. Kautsky, N. K. Nichols, and D. L. B. Jupp, "Smoothed histogram modification for image processing," *Comput. Vis., Graph., Image Process.*, vol. 26, no. 3, pp. 271–291, Jun. 1984.
- [21] V. R. Algazi and G. E. Ford, "Radiometric equalization of nonperiodic striping in satellite data," *Comput. Graph. Image Process.*, vol. 16, no. 3, pp. 287–295, Jul. 1981.
- [22] M. P. Weinreb, R. Xie, J. H. Lienesch, and D. S. Crosby, "Destriping GOES images by matching empirical distribution functions," *Remote Sens. Environ.*, vol. 29, no. 2, pp. 185–195, Aug. 1989.
- [23] L. Sun, R. Neville, K. Staenz, and H. P. White, "Automatic destriping of hyperion imagery based on spectral moment matching," *Can. J. Remote Sens.*, vol. 34, no. sup1, pp. S68–S81, Jun. 2014.
- [24] P. Rakwatin, W. Takeuchi, and Y. Yasuoka, "Stripe noise reduction in MODIS data by combining histogram matching with facet filter," *IEEE Trans. Geosci. Remote Sens.*, vol. 45, no. 6, pp. 1844–1856, Jun. 2007.
- [25] M. Wegener, "Destriping multiple sensor imagery by improved histogram matching," *Int. J. Remote Sens.*, vol. 11, no. 5, pp. 859–875, May 1990.
- [26] Y. Chang, L. Yan, T. Wu, and S. Zhong, "Remote sensing image stripe noise removal: From image decomposition perspective," *IEEE Trans. Geosci. Remote Sens.*, vol. 54, no. 12, pp. 7018–7031, Dec. 2016.
- [27] H. Shen and L. Zhang, "A MAP-based algorithm for destriping and inpainting of remotely sensed images," *IEEE Trans. Geosci. Remote Sens.*, vol. 47, no. 5, pp. 1492–1502, May 2009.
- [28] M. Bouali and S. Ladjal, "Toward optimal destriping of MODIS data using a unidirectional variational model," *IEEE Trans. Geosci. Remote Sens.*, vol. 49, no. 8, pp. 2924–2935, Aug. 2011.
- [29] G. Zhou, H. Fang, L. Yan, T. Zhang, and J. Hu, "Removal of stripe noise with spatially adaptive unidirectional total variation," *Optik*, vol. 125, no. 12, pp. 2756–2762, Jun. 2014.
- [30] Y. Chang, L. Yan, H. Fang, and C. Luo, "Anisotropic spectral-spatial total variation model for multispectral remote sensing image destriping," *IEEE Trans. Image Process.*, vol. 24, no. 6, pp. 1852–1866, Jun. 2015.
- [31] G. Zhou, H. Fang, C. Lu, S. Wang, Z. Zuo, and J. Hu, "Robust destriping of MODIS and hyperspectral data using a hybrid unidirectional total variation model," *Optik*, vol. 126, nos. 7–8, pp. 838–845, Apr. 2015.
- [32] M. Wang, X. Zheng, J. Pan, and B. Wang, "Unidirectional total variation destriping using difference curvature in MODIS emissive bands," *Infr. Phys. Technol.*, vol. 75, pp. 1–11, Mar. 2016.
- [33] X. Liu, X. Lu, H. Shen, Q. Yuan, Y. Jiao, and L. Zhang, "Stripe noise separation and removal in remote sensing images by consideration of the global sparsity and local variational properties," *IEEE Trans. Geosci. Remote Sens.*, vol. 54, no. 5, pp. 3049–3060, May 2016.

- [34] Y. Chen, T.-Z. Huang, L.-J. Deng, X.-L. Zhao, and M. Wang, "Group sparsity based regularization model for remote sensing image stripe noise removal," *Neurocomputing*, vol. 267, pp. 95–106, Dec. 2017.
- [35] X. Lu, Y. Wang, and Y. Yuan, "Graph-regularized low-rank representation for destriping of hyperspectral images," *IEEE Trans. Geosci. Remote Sens.*, vol. 51, no. 7, pp. 4009–4018, Jul. 2013.
- [36] Y. Chen, T.-Z. Huang, and X.-L. Zhao, "Destriping of multispectral remote sensing image using low-rank tensor decomposition," *IEEE J. Sel. Topics Appl. Earth Observ. Remote Sens.*, vol. 11, no. 12, pp. 4950–4967, Dec. 2018.
- [37] Y. Chang, L. Yan, X.-L. Zhao, H. Fang, Z. Zhang, and S. Zhong, "Weighted low-rank tensor recovery for hyperspectral image restoration," *IEEE Trans. Cybern.*, vol. 50, no. 11, pp. 4558–4572, Nov. 2020.
- [38] Y. Chang, L. Yan, B. Chen, S. Zhong, and Y. Tian, "Hyperspectral image restoration: Where does the low-rank property exist," *IEEE Trans. Geosci. Remote Sens.*, early access, Oct. 6, 2020, doi: [10.1109/TGRS.2020.3024623](https://doi.org/10.1109/TGRS.2020.3024623).
- [39] Y. Chang, M. Chen, L. Yan, X.-L. Zhao, Y. Li, and S. Zhong, "Toward universal stripe removal via wavelet-based deep convolutional neural network," *IEEE Trans. Geosci. Remote Sens.*, vol. 58, no. 4, pp. 2880–2897, Apr. 2020.
- [40] Q. Zhang, Q. Yuan, J. Li, X. Liu, H. Shen, and L. Zhang, "Hybrid noise removal in hyperspectral imagery with a spatial-spectral gradient network," *IEEE Trans. Geosci. Remote Sens.*, vol. 57, no. 10, pp. 7317–7329, Oct. 2019.
- [41] H. Zhang, W. He, L. Zhang, H. Shen, and Q. Yuan, "Hyperspectral image restoration using low-rank matrix recovery," *IEEE Trans. Geosci. Remote Sens.*, vol. 52, no. 8, pp. 4729–4743, Aug. 2014.
- [42] H. Fan, J. Li, Q. Yuan, X. Liu, and M. Ng, "Hyperspectral image denoising with bilinear low rank matrix factorization," *Signal Process.*, vol. 163, pp. 132–152, Oct. 2019.
- [43] J. Wright, A. Ganesh, S. Rao, Y. Peng, and Y. Ma, "Robust principal component analysis: Exact recovery of corrupted low-rank matrices via convex optimization," in *Proc. NIPS*, 2009, pp. 2080–2088.
- [44] Z. Zhou, X. Li, J. Wright, E. Candes, and Y. Ma, "Stable principal component pursuit," in *Proc. IEEE Int. Symp. Inf. Theory*, Jun. 2010, pp. 1518–1522.
- [45] M.-D. Iordache, J. Bioucas-Dias, and A. Plaza, "Sparse unmixing of hyperspectral data," *IEEE Trans. Geosci. Remote Sens.*, vol. 49, no. 6, pp. 2014–2039, Jun. 2011.
- [46] T. Xie, S. Li, and B. Sun, "Hyperspectral images denoising via non-convex regularized low-rank and sparse matrix decomposition," *IEEE Trans. Image Process.*, vol. 29, pp. 44–56, Jul. 2020.
- [47] F. L. Gadallah, F. Csillag, and E. J. M. Smith, "Destriping multisensor imagery with moment matching," *Int. J. Remote Sens.*, vol. 21, no. 12, pp. 2505–2511, Jan. 2000.
- [48] R. J. Hodrick and E. C. Prescott, "Postwar us business cycles: An empirical investigation," *J. Money Credit Bank.*, pp. 1–16, Feb. 1997.
- [49] A. Maravall and A. Del Rio, "Temporal aggregation, systematic sampling, and the Hodrick–Prescott filter," *Comput. Stat. Data Anal.*, vol. 52, no. 2, pp. 975–998, Aug. 2007.
- [50] S.-J. Kim, K. Koh, S. Boyd, and D. Gorinevsky, " $\ell_1$  trend filtering," *SIAM Rev.*, vol. 51, no. 2, pp. 339–360, 2009.
- [51] R. J. Tibshirani, "Adaptive piecewise polynomial estimation via trend filtering," *Ann. Statist.*, vol. 42, no. 1, pp. 285–323, Feb. 2014.
- [52] P. Rodriguez and B. Wohlberg, "Efficient minimization method for a generalized total variation functional," *IEEE Trans. Image Process.*, vol. 18, no. 2, pp. 322–332, Feb. 2009.
- [53] Z. Lin, R. Liu, and Z. Su, "Linearized alternating direction method with adaptive penalty for low-rank representation," in *Proc. NIPS*, 2011, pp. 612–620.
- [54] J.-F. Cai, E. J. Candès, and Z. Shen, "A singular value thresholding algorithm for matrix completion," *SIAM J. Optim.*, vol. 20, no. 4, pp. 1956–1982, Jan. 2010.
- [55] Z. Lin, M. Chen, and Y. Ma, "The augmented Lagrange multiplier method for exact recovery of corrupted low-rank matrices," 2010, *arXiv:1009.5055*. [Online]. Available: <http://arxiv.org/abs/1009.5055>
- [56] W. He, H. Zhang, H. Shen, and L. Zhang, "Hyperspectral image denoising using local low-rank matrix recovery and global spatial-spectral total variation," *IEEE J. Sel. Topics Appl. Earth Observ. Remote Sens.*, vol. 11, no. 3, pp. 713–729, Mar. 2018.
- [57] Y. Chen, X. Cao, Q. Zhao, D. Meng, and Z. Xu, "Denoising hyperspectral image with non-i.i.d. Noise structure," *IEEE Trans. Cybern.*, vol. 48, no. 3, pp. 1054–1066, Mar. 2018.
- [58] Q. Huynh-Thu and M. Ghanbari, "Scope of validity of PSNR in image/video quality assessment," *Electron. Lett.*, vol. 44, no. 13, pp. 800–801, Jun. 2008.
- [59] Z. Wang, A. C. Bovik, H. R. Sheikh, and E. P. Simoncelli, "Image quality assessment: From error visibility to structural similarity," *IEEE Trans. Image Process.*, vol. 13, no. 4, pp. 600–612, Apr. 2004.
- [60] R. H. Yuhas, A. F. Goetz, and J. W. Boardman, "Discrimination among semi-arid landscape endmembers using the spectral angle mapper (SAM) algorithm," in *Summaries 3rd Annu. JPL Airborne Geosci. Workshop*, 1992, pp. 147–149.
- [61] R. Vondrak, J. Keller, G. Chin, and J. Garvin, "Lunar reconnaissance orbiter (LRO): Observations for lunar exploration and science," *Space Sci. Rev.*, vol. 150, nos. 1–4, pp. 7–22, Feb. 2010.
- [62] D. E. Smith *et al.*, "Initial observations from the lunar orbiter laser altimeter (LOLA)," *Geophys. Res. Lett.*, vol. 37, no. 18, Sep. 2010, Art. no. L18204.
- [63] C. Li *et al.*, "Chang'e-4 initial spectroscopic identification of lunar far-side mantle-derived materials," *Nature*, vol. 569, no. 7756, pp. 378–382, May 2019.
- [64] K. Di *et al.*, "Topographic evolution of von Kármán crater revealed by the lunar rover Yutu-2," *Geophys. Res. Lett.*, vol. 46, no. 22, pp. 12764–12770, Nov. 2019.
- [65] X. Hu *et al.*, "Mineral abundances inferred from *in situ* reflectance measurements at the Chang'E-4 landing site in South Pole-Aitken basin," *Geophys. Res. Lett.*, vol. 46, no. 16, pp. 9439–9447, Aug. 2019.
- [66] L. Xiao *et al.*, "A young multilayered terrane of the northern mare imbrium revealed by Chang'E-3 mission," *Science*, vol. 347, no. 6227, pp. 1226–1229, Mar. 2015.
- [67] A. W. Gifford, T. A. Maxwell, and F. El-Baz, "Geology of the lunar far-side crater necho," *Moon Planets*, vol. 21, no. 1, pp. 25–42, Aug. 1979.
- [68] J. E. Nichol and V. Vohora, "Noise over water surfaces in Landsat TM images," *Int. J. Remote Sens.*, vol. 25, no. 11, pp. 2087–2093, Jun. 2004.
- [69] L. C. Cheek *et al.*, "The Goldschmidt region as viewed from moon mineralogy mapper (M<sup>3</sup>) data," in *Proc. 41th 8th Lunar Planet. Sci. Conf.*, Mar. 2010, p. 1962.
- [70] S. Besse *et al.*, "Compositional variability of the marius hills volcanic complex from the moon mineralogy mapper (M<sup>3</sup>)," *J. Geophys. Res.*, vol. 116, May 2011, Art. no. E00G13.
- [71] K. Tan *et al.*, "Vicarious calibration for the AHSI instrument of Gaofen-5 with reference to the CRCS Dunhuang test site," *IEEE Trans. Geosci. Remote Sens.*, early access, Aug. 18, 2020, doi: [10.1109/TGRS.2020.3014656](https://doi.org/10.1109/TGRS.2020.3014656).
- [72] Z. Ouyang *et al.*, "Chang'E-1 lunar mission: An overview and primary science results," *Chin. J. Cancer Space Sci.*, vol. 30, no. 5, pp. 392–403, 2010.
- [73] Y. Wu *et al.*, "Global estimates of lunar iron and titanium contents from the Chang'E-1 IIM data," *J. Geophys. Res., Planets*, vol. 117, no. E2, pp. 1–23, Feb. 2012.
- [74] Y. Wu *et al.*, "Photometric correction and in-flight calibration of Chang'E-1 interference imaging spectrometer (IIM) data," *Icarus*, vol. 222, no. 1, pp. 283–295, Jan. 2013.
- [75] Y. Wu, "Major elements and Mg# of the moon: Results from Chang'E-1 interference imaging spectrometer (IIM) data," *Geochimica et Cosmochimica Acta*, vol. 93, pp. 214–234, Sep. 2012.
- [76] C. M. Pieters *et al.*, "Character and spatial distribution of OH/H<sub>2</sub>O on the surface of the moon seen by M<sup>3</sup> on Chandrayaan-1," *Science*, vol. 326, no. 5952, pp. 568–572, Oct. 2009.
- [77] X.-Y. Zhang *et al.*, "Study of the continuum removal method for the moon mineralogy mapper (M<sup>3</sup>) and its application to mare humorum and mare nubium," *Res. Astron. Astrophys.*, vol. 16, no. 7, p. 115, Jul. 2016.



**Shuheng Zhao** received the B.S. degree in geodesy and geomatics engineering from Wuhan University, Wuhan, China, in 2018, where she is pursuing the M.S. degree with the State Key Laboratory of Information Engineering in Surveying, Mapping, and Remote Sensing (LIESMARS).

Her research interests include planetary remote sensing and hyperspectral image processing.



**Qiangqiang Yuan** (Member, IEEE) received the B.S. degree in surveying and mapping engineering and the Ph.D. degree in photogrammetry and remote sensing from Wuhan University, Wuhan, China, in 2006 and 2012, respectively.

In 2012, he joined the School of Geodesy and Geomatics, Wuhan University, where he is a Professor. He has authored more than 90 research papers, including more than 70 peer-reviewed articles in international journals such as the *Remote Sensing of Environment*, *ISPRS Journal of Photogrammetry and Remote Sensing*, IEEE TRANSACTIONS IMAGE PROCESSING, and IEEE TRANSACTIONS ON GEOSCIENCE AND REMOTE SENSING. His research interests include image reconstruction, remote sensing image processing and application, and data fusion.

Dr. Yuan was a recipient of the Youth Talent Support Program of China in 2019, and the Top-Ten Academic Star of Wuhan University in 2011. In 2014, he received the Hong Kong Scholar Award from the Society of Hong Kong Scholars and the China National Postdoctoral Council. He is the Associate Editor of five international journals and has frequently served as a referee for more than 40 international journals for remote sensing and image processing. He was a recipient of the recognition of Best Reviewers of the IEEE GEOSCIENCE AND REMOTE SENSING LETTERS in 2019.



**Jie Li** (Member, IEEE) received the B.S. degree in sciences and techniques of remote sensing and the Ph.D. degree in photogrammetry and remote sensing from Wuhan University, Wuhan, China, in 2011 and 2016, respectively.

He is an Associate Professor with the School of Geodesy and Geomatics, Wuhan University. His research interests include image quality improvement, image super-resolution reconstruction, data fusion, remote sensing image processing, sparse representation, and deep learning.



**Yunze Hu** received the B.S. degree in geodesy and geomatics engineering from Wuhan University, Wuhan, China, in 2020, where she is pursuing the M.S. degree with the School of Geodesy and Geomatics.

Her research interests include planetary remote sensing and crater automatic detection.



**Xinxin Liu** received the B.S. degree in geographic information system and the Ph.D. degree in cartography and geographic information system from Wuhan University, Wuhan, China, in 2013 and 2018, respectively.

In July 2018, she joined the College of Electrical and Information Engineering, Hunan University, Changsha, China, where she is an Assistant Professor. Her research interests include image quality improvement, remote sensing image processing, and remote sensing mapping and application.



**Liangpei Zhang** (Fellow, IEEE) received the B.S. degree in physics from Hunan Normal University, Changsha, China, in 1982, the M.S. degree in optics from the Xi'an Institute of Optics and Precision Mechanics, Chinese Academy of Sciences, Xi'an, China, in 1988, and the Ph.D. degree in photogrammetry and remote sensing from Wuhan University, Wuhan, China, in 1998.

He was a Principal Scientist for the China State Key Basic Research Project (2011–2016) appointed by the Ministry of National Science and Technology of China to Lead the Remote Sensing Program in China. He is a Chair Professor with the State Key Laboratory of Information Engineering in Surveying, Mapping, and Remote Sensing (LIESMARS), Wuhan University. He has authored more than 700 research papers and 5 books. He is the Institute for Scientific Information (ISI) highly cited author. He is the holder of 30 patents. His research interests include hyperspectral remote sensing, high-resolution remote sensing, image processing, and artificial intelligence.

Dr. Zhang is a fellow of the Institution of Engineering and Technology (IET). He was a recipient of the 2010 Best Paper Boeing Award, the 2013 Best Paper ERDAS Award from the American Society of Photogrammetry and Remote Sensing (ASPRS), and the 2016 Best Paper Theoretical Innovation Award from the International Society for Optics and Photonics (SPIE). His research teams won the top three prizes of the IEEE Geoscience and Remote Sensing Society (GRSS) 2014 Data Fusion Contest, and his students have been selected as the winners or finalists of the IEEE International Geoscience and Remote Sensing Symposium (IGARSS) student paper contest in recent years. He also serves as an Associate Editor or Editor for more than ten international journals. He is also serving as an Associate Editor for the IEEE TRANSACTIONS ON GEOSCIENCE AND REMOTE SENSING. He is the Founding Chair of the IEEE GRSS Wuhan Chapter.